

1 **STABLE ASYMMETRIC SPIKE EQUILIBRIA FOR THE**
2 **GIERER-MEINHARDT MODEL WITH A PRECURSOR FIELD**

3 THEODORE KOLOKOLNIKOV ^{*}, FRÉDÉRIC PAQUIN-LEFEBVRE [†], AND MICHAEL J.
4 WARD [‡]

5 **Abstract.** Precursor gradients in a reaction-diffusion system are spatially varying coefficients
6 in the reaction-kinetics. Such gradients have been used in various applications, such as the head
7 formation in the Hydra, to model the effect of pre-patterns and to localize patterns in various spatial
8 regions. For the 1-D Gierer-Meinhardt (GM) model we show that a simple precursor gradient in
9 the decay rate of the activator can lead to the existence of stable, asymmetric, two-spike patterns,
10 corresponding to localized peaks in the activator of different heights. This is a qualitatively new
11 phenomena for the GM model, in that asymmetric spike patterns are all unstable in the absence of
12 the precursor field. Through a determination of the global bifurcation diagram of two-spike steady-
13 state patterns, we show that asymmetric patterns emerge from a supercritical symmetry-breaking
14 bifurcation along the symmetric two-spike branch as a parameter in the precursor field is varied.
15 Through a combined analytical-numerical approach we analyze the spectrum of the linearization
16 of the GM model around the two-spike steady-state to establish that portions of the asymmetric
17 solution branches are linearly stable. In this linear stability analysis a new class of vector-valued
18 nonlocal eigenvalue problem (NLEP) is derived and analyzed.

19 **1. Introduction.** We analyze the existence, linear stability, and bifurcation
20 behavior of localized steady-state spike patterns for the Gierer-Meinhardt reaction-
21 diffusion (RD) model in a 1-D domain where we have included a spatially variable
22 coefficient for the decay rate of the activator. We will show that this spatial hetero-
23 geneity in the model, referred to as a precursor gradient, can lead to the existence of
24 stable *asymmetric* two-spike equilibria, corresponding to steady-state spikes of differ-
25 ent height (see the right panel of Fig. 2). This is a qualitatively new phenomenon for
26 the GM model since, in the absence of a precursor field, asymmetric steady-state spike
27 patterns for the GM model are always unstable [29]. A combination of analytical and
28 numerical methods is used to determine parameter ranges where stable asymmetric
29 steady-state patterns for the GM model with a simple precursor field can occur. We
30 will show that these stable asymmetric equilibria emerge from a symmetry-breaking
31 supercritical pitchfork bifurcation of symmetric spike equilibria as a parameter in the
32 precursor field is varied.

33 Precursor gradients have been used in various specific applications of RD theory
34 since the initial study by Gierer and Meinhardt in [8] for modeling head development
35 in the Hydra. For other RD systems, precursor gradients have also been used in the
36 numerical simulations of [11] to model the formation and localization of heart tissue
37 in the Axolotl, which is a type of salamander. Further applications of such gradients
38 for the GM model and other RD systems are discussed in [11], [12], [21], and [9].
39 With a precursor field, or with spatially variable diffusivities, the RD system does not
40 generally admit a spatially uniform state. As a result, a conventional Turing stability
41 approach is not applicable and the initial development of small amplitude patterns
42 must be analyzed through either a slowly-varying assumption or from full numerical
43 simulations (cf. [13], [22], [23], [20]).

44 In contrast to small amplitude patterns, in the singularly perturbed limit of a
45 large diffusivity ratio $\mathcal{O}(\varepsilon^{-2}) \gg 1$, many two-component RD systems in 1-D admit

^{*}Department of Mathematics and Statistics, Dalhousie University, Halifax, Canada. (corresponding author tkolokol@gmail.com)

[†]Department of Mathematics, UBC, Vancouver, Canada. (paquinl@math.ubc.ca)

[‡]Department of Mathematics, UBC, Vancouver, Canada. (ward@math.ubc.ca)

46 spike-type solutions. In this direction, there is a rather extensive analytical theory on
 47 the existence, linear stability and slow dynamics of spike-type solutions for many such
 48 RD systems in 1-D (see [5], [6], [14], [15], [24] [25], [26], and the references therein).
 49 To establish parameter regimes where spike-layer steady-states are linearly stable,
 50 one must analyze the spectrum of the operator associated with a linearization around
 51 the spike-layer solution. In this spectral analysis one must consider both the small
 52 eigenvalues of order $\mathcal{O}(\varepsilon^2)$ associated with near-translation invariance and the large
 53 $\mathcal{O}(1)$ eigenvalues that characterize any instabilities in the amplitudes of the spikes.
 54 These latter eigenvalues are associated with nonlocal eigenvalue problems (NLEPs),
 55 for which many rigorous results are available (cf. [4], [30], [28]).

56 Despite these advances, the effect of spatially heterogeneous coefficients in the
 57 reaction kinetics on spike existence, stability, and dynamics is much less well under-
 58 stood. With a precursor gradient, spike pinning can occur for the GM model (cf. [27],
 59 [31]) and for the Fitzhugh-Nagumo model (cf. [2], [10]), while a plant hormone (auxin)
 60 gradient is predicted to control the spatial locations of root formation in plant cells
 61 [1]. In other contexts, a spatial heterogeneity can trigger a self-replication loop con-
 62 sisting of spike formation, propagation, and annihilation against a domain boundary
 63 [19]. More recently, clusters of spikes that are confined as a result of a spatial het-
 64 erogeneity have been analyzed in 1-D in [16] and [18] for the GM and Schnakenberg
 65 models, respectively, and in [17] for 2-D spot clusters of the GM model. In these
 66 recent approaches the RD system with clustered spikes is effectively approximated by
 67 a limiting equation for the spike density.

68 In our study we will consider the dimensionless GM model in 1-D with activator
 69 a and inhibitor h , and with a smooth precursor $\mu(x) > 0$ in the decay rate of the
 70 activator, given for $\varepsilon \ll 1$ by

$$71 \quad (1.1a) \quad a_t = \varepsilon^2 a_{xx} - \mu(x)a + \frac{a^2}{h}, \quad |x| < L, \quad t > 0; \quad a_x(\pm L, t) = 0,$$

$$73 \quad (1.1b) \quad \tau h_t = h_{xx} - h + \varepsilon^{-1} a^2, \quad |x| < L, \quad t > 0; \quad h_x(\pm L, t) = 0.$$

74 Although our analytical framework can be applied more generally, we will exhibit
 75 stable asymmetric spike-layer steady-states only for the specific precursor field

$$76 \quad (1.2) \quad \mu(x) = 1 + bx^2,$$

77 where $b > 0$ is a bifurcation parameter. In our formulation in (1.1), we have for
 78 convenience fixed the inhibitor diffusivity at unity and will use the domain length L
 79 as the other bifurcation parameter.

80 In §2 we use a matched asymptotic approach to derive a differential algebraic
 81 system of ODEs (DAEs) for a collection of spikes for (1.1), under the assumption that
 82 the quasi-equilibrium spike pattern is stable on $\mathcal{O}(1)$ time-scales. The DAE system
 83 is written in terms of 1-D Green's functions, or equivalently as a tridiagonal system.
 84 In §3 we provide two alternative approaches for computing global branches of two-
 85 spike equilibria of the DAE system, for the μ as given in (1.2), and we formulate a
 86 generalized matrix eigenvalue problem characterizing the linear stability of branches
 87 of equilibria. Numerical results for steady-state spike locations and spike heights,
 88 denoting maxima of the inhibitor field, corresponding to global bifurcation branches
 89 of two-spike equilibria are shown in §3.2 in terms of the precursor parameter b and the
 90 domain half-length L . We show that the asymmetric branches of two-spike equilibria
 91 emerge from a symmetry breaking pitchfork bifurcation from the symmetric branch at
 92 a critical value $b = b_p(L)$. For $b > 0.076$, we show that this bifurcation is supercritical,

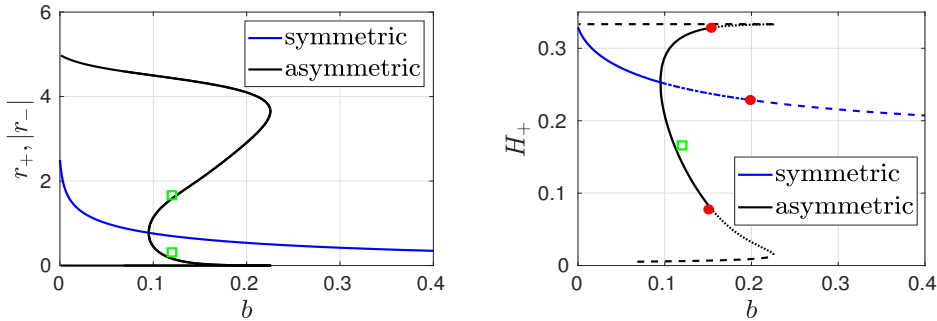


Fig. 1: Left: steady-state spike locations $x_1 = -r_-$ and $x_2 = r_+$ for $L = 5$ versus b in (1.2). Right: height H_+ of the rightmost spike versus b . Solid lines: linearly stable to both the small eigenvalues and the large (NLEP) eigenvalues when $\tau \ll 1$. Dash-dotted lines: unstable for the small eigenvalues but stable for the large eigenvalues when $\tau \ll 1$. Dashed line: stable to the small eigenvalues but unstable to the large eigenvalues when $\tau \ll 1$. Dotted line: unstable to both the small and large eigenvalues when $\tau \ll 1$. Red dots: zero-eigenvalue crossings for the NLEP. Green squares: the stable steady-state observed in the full PDE simulation of (1.1) shown in Fig. 2.

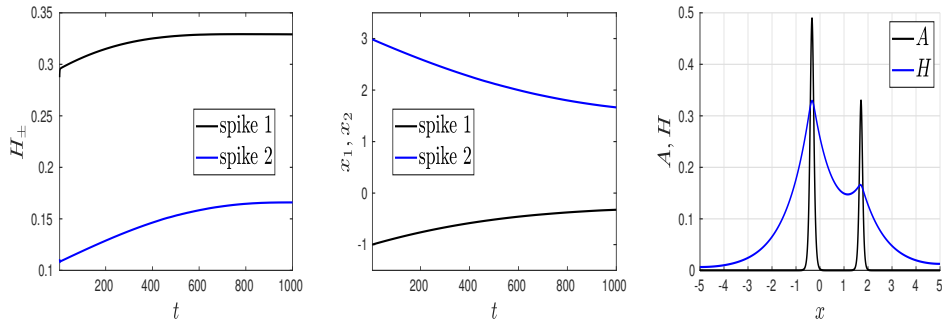


Fig. 2: Time-dependent PDE simulations of (1.1) with $L = 5$, $\varepsilon = 0.05$, and $\tau = 0.25$ for a precursor $\mu(x) = 1 + bx^2$ with $b = 0.12$. Initial condition is a quasi-equilibrium two-spike solution with spike locations $x_1(0) = -1$ and $x_2(0) = 3$. Spike heights (left panel), denoting maxima of the inhibitor field, and spike locations (middle panel) versus time. Right: the steady-state asymmetric two-spike equilibrium, stable to the small and large eigenvalues, corresponding to the green squares in Fig. 1.

93 and that the bifurcating branches of asymmetric equilibria are linearly stable as a
94 steady-state solution of the DAE dynamics.

95 In §4 we derive a vector-valued NLEP characterizing spike amplitude instabilities
96 of steady-state spike patterns of (1.1). For the case of symmetric two-spike equilibria,
97 the vector-valued NLEP can be diagonalized, and we obtain necessary and sufficient
98 conditions for the linear stability of these patterns when τ in (1.1) is sufficiently small.
99 The resulting stability thresholds are shown in the global bifurcation plots in §3.2.
100 However, for asymmetric two-spike equilibria, we obtain a new vector-valued NLEP

that cannot be diagonalized, and for which the NLEP stability results in [30] are not directly applicable. For this new NLEP we determine analytically parameter values corresponding to zero-eigenvalue crossings, and for $\tau = 0$ we numerically compute any unstable eigenvalues by using a discretization of the vector-valued NLEP combined with a generalized matrix eigenvalue solver.

In 5 we confirm our global bifurcation and linear stability results through full PDE simulations of (1.1). As an illustration of our results, in Fig. 1 we plot the spike locations and spike heights corresponding to steady-state branches of symmetric and asymmetric two-spike equilibria in terms of the precursor parameter b for a domain half-length $L = 5$. The two branches of asymmetric two-spike equilibria result from an even reflection of solutions through the origin $x = 0$. In the right panel of Fig. 1, where we plot the spike heights, we show the linear stability properties for the small eigenvalues, as obtained from the linearization of the DAE system, and for the large eigenvalues, as determined from computations of the vector-valued NLEP. The time-dependent PDE simulations shown in Fig. 2 confirm that a quasi-equilibrium two-spike pattern tends to a stable asymmetric equilibrium on a long time scale. The paper concludes with a brief discussion in §6.

2. Derivation of the DAE System. We now derive a DAE system for the spike locations for an N -spike quasi-equilibrium pattern, which is valid in the absence of any $\mathcal{O}(1)$ time-scale instability of the pattern. Since this analysis is similar to that given in [15] with no precursor field and in [27] for a precursor field, but with only one spike, we only briefly outline the analysis here.

The spike locations x_j , for $j = 1, \dots, N$, are assumed to satisfy $|x_{j+1} - x_j| \gg \mathcal{O}(\varepsilon)$, with $|x_1 + L| \gg \mathcal{O}(\varepsilon)$ and $|L - x_N| \gg \mathcal{O}(\varepsilon)$. As shown in [15] and [27], in the absence of any $\mathcal{O}(1)$ time-scale instability of the spike amplitudes, the spikes will evolve on the long time-scale $\sigma = \varepsilon^2 t$, and so we write $x_j = x_j(\sigma)$.

To derive a DAE system for $x_j(\sigma)$, for $j = 1, \dots, N$, we first construct the solution in the inner region near the j -th spike. We introduce the inner expansion

$$(2.1) \quad a = A_0 + \varepsilon A_1 + \dots, \quad h = H_0 + \varepsilon H_1 + \dots,$$

where $A_i = A_i(y, \sigma)$ and $H_i = H_i(y, \sigma)$ for $i = 0, 1$ and $y = \varepsilon^{-1}(x - x_j)$. Upon substituting (2.1) into (1.1), and using $a_t = -\varepsilon x'_j A_{0y} + \mathcal{O}(\varepsilon^2)$ where $x'_j \equiv dx_j/d\sigma$, we collect powers of ε to obtain the following leading-order problem on $-\infty < y < \infty$:

$$(2.2) \quad A_{0yy} - \mu_j A_0 + A_0^2/H_0 = 0, \quad H_{0yy} = 0,$$

where $\mu_j \equiv \mu(x_j)$. At next order, we conclude on $-\infty < y < \infty$ that

$$(2.3a) \quad \mathcal{L}A_1 \equiv A_{1yy} - \mu_j A_1 + \frac{2A_0}{H_0} A_1 = \frac{A_0^2}{H_0^2} H_1 + y\mu'(x_j) A_0 - x'_j A_{0y},$$

$$(2.3b) \quad H_{1yy} = -A_0^2.$$

From (2.2) we get that $H_0 = H_{0j}(\sigma)$, where H_{0j} , independent of y , is to be determined. In addition, the spike profile is given by

$$(2.4) \quad A_0 = \mu_j H_{0j} w(\sqrt{\mu_j} y) \quad \text{where} \quad w(z) = \frac{3}{2} \operatorname{sech}^2(z/2),$$

where $w(0) > 0$ with $w'(0) = 0$, is the well-known homoclinic solution to

$$(2.5) \quad w'' - w + w^2 = 0, \quad -\infty < z < \infty, \quad w \rightarrow 0 \quad \text{as} \quad |z| \rightarrow \infty.$$

144 Since $\mathcal{L}A_{0y} = 0$, the solvability condition for (2.3a) is that

$$\begin{aligned} 145 \quad (2.6) \quad x'_j \int A_{0y}^2 dy &= \mu'(x_j) \int y A_0 A_{0y} dy + \int \frac{A_0^2}{H_{0j}^2} H_1 A_{0y} dy \\ &= \frac{\mu'(x_j)}{2} \int y (A_0^2)_y dy + \frac{1}{3H_{0j}^2} \int (A_0^3)_y H_1 dy \\ &= -\frac{\mu'(x_j)}{2} \int A_0^2 dy - \frac{1}{3H_{0j}^2} \int A_0^3 H_{1y} dy, \end{aligned}$$

146 where we have used integration by parts and the shorthand notation $\int = \int_{-\infty}^{\infty}$. From
147 a further integration by parts on the last term on the last line in (2.6), and using the
148 fact that $H_{1yy} = -A_0^2$ is even, we obtain that

$$149 \quad (2.7) \quad x'_j = -\frac{\mu'(x_j)}{2} I_1 - \frac{1}{6H_{0j}^2} I_2 \left(\lim_{y \rightarrow +\infty} H_{1y} + \lim_{y \rightarrow -\infty} H_{1y} \right),$$

150 in terms of the integral ratios I_1 and I_2 defined by

$$151 \quad (2.8) \quad I_1 \equiv \frac{\int A_0^2 dy}{\int A_{0y}^2 dy}, \quad I_2 \equiv \frac{\int A_0^3 dy}{\int A_{0y}^2 dy}.$$

152 By multiplying the ODE for A_0 in (2.2) first by A_{0y} and then by A_0 , we integrate the
153 two resulting expressions to obtain an algebraic system for I_1 and I_2 , which yields

$$154 \quad (2.9) \quad I_1 = \frac{5}{\mu_j}, \quad I_2 = 6H_{0j}.$$

155 Upon using (2.9) in (2.7), we conclude for each $j = 1, \dots, N$ that

$$156 \quad (2.10) \quad x'_j = -\frac{5}{2} \frac{\mu'(x_j)}{\mu(x_j)} - \frac{1}{H_{0j}} \left(\lim_{y \rightarrow +\infty} H_{1y} + \lim_{y \rightarrow -\infty} H_{1y} \right).$$

157 To determine H_{0j} for $j = 1, \dots, N$ and the remaining term in (2.10) we need to
158 determine the outer solution.

159 Now in the outer region, defined away from $\mathcal{O}(\varepsilon)$ regions near each x_j , a is ex-
160ponentially small. In the sense of distributions we then use $A_0 = H_{0j}\mu_j w(\sqrt{\mu_j}y)$ to
161 calculate across each $x = x_j$ that

$$\begin{aligned} 162 \quad (2.11) \quad \frac{1}{\varepsilon} a^2 &\rightarrow \left(\int A_0^2 dy \right) \delta(x - x_j) = \mu_j^{3/2} H_{0j}^2 \left(\int w^2(z) dz \right) \delta(x - x_j) = 6\mu_j^{3/2} H_{0j}^2 \delta(x - x_j), \end{aligned}$$

163 owing to the fact that $\int w^2 z = \int w dz = 6$. In this way, the outer problem for h is

$$164 \quad (2.12) \quad h_{xx} - h = -6 \sum_{j=1}^N H_{0j}^2 \mu_j^{3/2} \delta(x - x_j), \quad |x| \leq L; \quad h_x(\pm L, \sigma) = 0.$$

165 The solution to (2.12) is

$$166 \quad (2.13) \quad h(x) = \sum_{i=1}^N H_{0i}^2 \mu_i^{3/2} G(x; x_i),$$

167 where $G(x; x_i)$ is the 1-D Green's function satisfying

$$168 \quad (2.14) \quad G_{xx} - G = -\delta(x - x_i), \quad |x| \leq L; \quad G_x(\pm L; x_i) = 0.$$

169 To match with the inner solutions near each x_j , we require for each $j = 1, \dots, N$ that

$$170 \quad (2.15) \quad h(x_j) = H_{0j}, \quad \lim_{y \rightarrow \infty} H_{1y} + \lim_{y \rightarrow -\infty} H_{1y} = h_x(x_{j+}) + h_x(x_{j-}).$$

171 In this way, by using (2.15) in (2.13) and (2.10) we obtain the following DAE system
172 for slow spike motion:

$$173 \quad (2.16a) \quad \frac{dx_j}{d\sigma} = -\frac{5}{2} \frac{\mu'(x_j)}{\mu_j} - \frac{12}{H_j} \left(\mu_j^{3/2} H_j^2 \langle G_x \rangle_j + \sum_{\substack{i=1 \\ i \neq j}}^N \mu_i^{3/2} H_i^2 G_x(x_j; x_i) \right),$$

$$174 \quad (2.16b) \quad H_j = 6 \sum_{i=1}^N \mu_i^{3/2} H_i^2 G(x_j; x_i),$$

176 where $\mu_j \equiv \mu(x_j)$, $\langle G_x \rangle_j \equiv [G_x(x_{j+}; x_i) + G_x(x_{j-}; x_i)]/2$, and $G(x; x_j)$ is the Green's
177 function satisfying (2.14). In (2.16), we have relabeled H_{0j} by H_j .

178 A simple special case of (2.16) is for the infinite-line problem with $L \rightarrow \infty$, for
179 which $G(x; x_i) = \frac{1}{2}e^{-|x-x_i|}$. For this case, we calculate $\langle G_x \rangle_j = 0$ and $G_x(x_j; x_i) =$
180 $-\frac{1}{2}\text{sign}(x_j - x_i)e^{-|x_j - x_i|}$. In this way, we can rewrite (2.16) as

$$181 \quad (2.17a) \quad \frac{dx_j}{d\sigma} = -\frac{5}{2} \frac{\mu'(x_j)}{\mu_j} + \frac{1}{H_j} \sum_{\substack{i=1 \\ i \neq j}}^N S_i \text{sign}(x_j - x_i) e^{-|x_j - x_i|},$$

$$182 \quad (2.17b) \quad H_j = \frac{1}{2} \sum_{i=1}^N S_i e^{-|x_j - x_i|}, \quad H_j = \left(\frac{S_j}{6\mu_j^{3/2}} \right)^{1/2}.$$

185 From (2.16a), we observe that the DAE dynamics for the j -th spike is globally
186 coupled to all of the other spikes through full matrices. We now proceed as in [15] to
187 derive an equivalent representation of (2.16a) that is based only on nearest neighbor
188 interactions. To do so, we first write (2.16) compactly in matrix form as

$$189 \quad (2.18) \quad \frac{d\mathbf{x}}{d\sigma} = -\frac{5}{2} \boldsymbol{\mu}_p - 2\mathcal{H}^{-1} \mathcal{P} \mathcal{G}^{-1} \mathbf{h}, \quad \mathcal{G}^{-1} \mathbf{h} = 6 \mathcal{U} \mathbf{h}^2,$$

190 where \mathcal{G} and \mathcal{P} are defined in terms of the Green's function by

$$191 \quad (2.19a) \quad \mathcal{G} \equiv \begin{pmatrix} G(x_1; x_1) & \cdots & G(x_1; x_N) \\ \vdots & \ddots & \vdots \\ G(x_N; x_1) & \cdots & G(x_N; x_N) \end{pmatrix}, \quad \mathcal{P} \equiv \begin{pmatrix} \langle G_x \rangle_1 & \cdots & G_x(x_1; x_N) \\ \vdots & \ddots & \vdots \\ G_x(x_N; x_1) & \cdots & \langle G_x \rangle_N \end{pmatrix}.$$

192 In (2.18), \mathcal{U} and \mathcal{H} are diagonal matrices with diagonal entries $(\mathcal{U})_{jj} = \mu(x_j)$ and
193 $(\mathcal{H})_{jj} = H_j$ for $j = 1, \dots, N$, and we have defined

$$194 \quad (2.19b) \quad \mathbf{h} \equiv \begin{pmatrix} H_1 \\ \vdots \\ H_N \end{pmatrix}, \quad \mathbf{h}^2 \equiv \begin{pmatrix} H_1^2 \\ \vdots \\ H_N^2 \end{pmatrix}, \quad \boldsymbol{\mu}_p \equiv \begin{pmatrix} \frac{\mu'(x_1)}{\mu(x_1)} \\ \vdots \\ \frac{\mu'(x_N)}{\mu(x_N)} \end{pmatrix}.$$

195 As shown in Appendix A of [15] (see also Appendix A of [14]), the inverse $\mathcal{B} \equiv \mathcal{G}^{-1}$ of
 196 the Green's matrix and the product $\mathcal{P}\mathcal{G}^{-1}$ are each triangular matrices of the form
 (2.20a)

$$197 \quad \mathcal{B} = \begin{pmatrix} c_1 & d_1 & & 0 \\ d_1 & \ddots & \ddots & \\ & \ddots & \ddots & d_{N-1} \\ 0 & & d_{N-1} & c_N \end{pmatrix}, \quad 2\mathcal{P}\mathcal{B} \equiv \mathcal{A} = \begin{pmatrix} e_1 & -d_1 & & 0 \\ d_1 & \ddots & \ddots & \\ & \ddots & \ddots & -d_{N-1} \\ 0 & & d_{N-1} & e_N \end{pmatrix},$$

198 where the matrix entries are given by

(2.20b)

$$\begin{aligned} c_1 &= \coth(x_2 - x_1) + \tanh(L + x_1), & c_N &= \coth(x_N - x_{N-1}) + \tanh(L - x_N), \\ c_j &= \coth(x_{j+1} - x_j) + \coth(x_j - x_{j-1}), & j &= 2, \dots, N-1, \\ e_1 &= \tanh(L + x_1) - \coth(x_2 - x_1), & e_N &= \coth(x_N - x_{N-1}) - \tanh(L - x_N), \\ e_j &= \coth(x_j - x_{j-1}) - \coth(x_{j+1} - x_{j-1}), & j &= 2, \dots, N-1, \\ d_j &= -\operatorname{csch}(x_{j+1} - x_j), & j &= 1, \dots, N-1. \end{aligned}$$

200 For the infinite-line problem, we calculate for the limit $L \rightarrow \infty$ that

$$201 \quad (2.21) \quad \begin{aligned} c_1 &\rightarrow \frac{2}{1 - e^{-2(x_2 - x_1)}}, & c_N &\rightarrow \frac{2}{1 - e^{-2(x_N - x_{N-1})}}, & \text{as } L &\rightarrow \infty, \\ e_1 &\rightarrow \frac{2}{1 - e^{2(x_2 - x_1)}}, & e_N &\rightarrow -\frac{2}{1 - e^{2(x_N - x_{N-1})}}, & \text{as } L &\rightarrow \infty. \end{aligned}$$

202 Finally, upon substituting (2.20) into (2.18), we obtain the following more tractable,
 203 but equivalent, tridiagonal representation of the DAE dynamics (2.16):

$$204 \quad (2.22) \quad \frac{dx}{d\sigma} = -\frac{5}{2} \boldsymbol{\mu}_p - \mathcal{H}^{-1} \mathcal{A} \mathbf{h}, \quad \mathcal{B} \mathbf{h} = 6 \mathcal{U} \mathbf{h}^2.$$

205 **3. Global Bifurcation Diagram of Spike Equilibria.** In this section we
 206 analyze bifurcation behavior for two-spike equilibria of (2.22) and study their stability
 207 properties in terms of equilibrium points of the DAE system (2.22). From (2.22), the
 208 equilibria satisfy the nonlinear algebraic system $\mathcal{F}(x_1, x_2, H_1, H_2) = \mathbf{0}$ for $\mathcal{F} \in \mathbb{R}^4$,
 209 given component-wise by

$$210 \quad (3.1) \quad \begin{aligned} \mathcal{F}_1 &\equiv -\frac{5}{2} \frac{\mu'(x_1)}{\mu(x_1)} - e_1 + d_1 \frac{H_2}{H_1}, & \mathcal{F}_2 &\equiv -\frac{5}{2} \frac{\mu'(x_2)}{\mu(x_2)} - e_2 - d_1 \frac{H_1}{H_2}, \\ \mathcal{F}_3 &= 6 [\mu(x_1)]^{3/2} H_1^2 - c_1 H_1 - d_1 H_2, & \mathcal{F}_4 &= 6 [\mu(x_2)]^{3/2} H_2^2 - d_1 H_1 - c_2 H_2. \end{aligned}$$

211 The linear stability properties of an equilibrium state (r_+, r_-, H_+, H_-) of the DAE
 212 dynamics (2.22) is based on the eigenvalues ω of the matrix eigenvalue problem

$$213 \quad (3.2) \quad J\mathbf{v} = \omega \mathcal{D}\mathbf{v},$$

214 where $J \equiv D\mathcal{F}$ is the Jacobian of \mathcal{F} and \mathcal{D} is the rank-defective diagonal matrix with
 215 matrix entries $(\mathcal{D})_{11} = 1$, $(\mathcal{D})_{22} = 1$, $(\mathcal{D})_{33} = 0$, and $(\mathcal{D})_{44} = 0$. Since $\operatorname{rank}(\mathcal{D}) = 2$,
 216 (3.2) has two infinite eigenvalues. The signs of the real parts of the remaining two
 217 matrix eigenvalues classify the linear stability of the equilibrium point for (2.22).

218 We will refer to these eigenvalues as the “small eigenvalues” for spike stability in
 219 accordance with the term used in [14] in the absence of a precursor field.

220 We now outline a simple approach for computing branches of solutions to $\mathcal{F} = \mathbf{0}$
 221 in terms of a parameter in the precursor field $\mu(x)$. An alternative formulation is
 222 given in §3.1 below. For the first approach, we introduce the spike height ratio s by

$$223 \quad (3.3) \quad s \equiv \frac{H_2}{H_1},$$

224 and reduce (3.1) to the three-component system $\mathcal{N}(x_1, x_2, s) = 0$ with $\mathcal{N} \in \mathbb{R}^3$ defined
 225 by

$$226 \quad (3.4a) \quad \mathcal{N}_1 \equiv -\frac{5}{2} \frac{\mu'(x_1)}{\mu(x_1)} - e_1 + d_1 s, \quad \mathcal{N}_2 \equiv -\frac{5}{2} \frac{\mu'(x_2)}{\mu(x_2)} - e_2 - \frac{d_1}{s},$$

$$227 \quad (3.4b) \quad \mathcal{N}_3 = s^2 [\mu(x_2)]^{3/2} (c_1 + d_1 s) - [\mu(x_1)]^{3/2} (d_1 + c_2 s).$$

229 In terms of solutions to $\mathcal{N}_j = 0$ for $j = 1, \dots, 3$ the spike heights are

$$230 \quad (3.4c) \quad H_1 = \frac{(c_1 + d_1 s)}{6 [\mu(x_1)]^{3/2}}, \quad H_2 = s H_1.$$

231 In (3.4) and (3.1), the constants c_1, c_2, d_1, e_1 , and e_2 are defined by (see (2.20b)):

$$232 \quad (3.5) \quad \begin{aligned} c_1 &= \coth(x_2 - x_1) + \tanh(L + x_1), & c_2 &= \coth(x_2 - x_1) + \tanh(L - x_2), \\ e_1 &= \tanh(L + x_1) - \coth(x_2 - x_1), & e_2 &= \coth(x_2 - x_1) - \tanh(L - x_2), \\ d_1 &= -\operatorname{csch}(x_2 - x_1). \end{aligned}$$

233 For the special case where $\mu(x)$ is even, i.e. $\mu(x) = \mu(-x)$, we label “symmetric”
 234 spike equilibria as those solutions of (3.4) for which $s = 1$ and $x_2 = -x_1$. For
 235 this case, $c_1 = c_2$, $e_2 = -e_1$, and $\mathcal{N}_3(-x_2, x_2, 1) = 0$. Moreover, we calculate that
 236 $e_2 + d_1 = \tanh(x_2) - \tanh(L - x_2)$, and so (3.4) reduces to finding a root x_2 on
 237 $0 < x_2 < L$ to the scalar equation $\mathcal{S}(x_2) = 0$ given by

$$238 \quad (3.6) \quad \mathcal{S}(x_2) \equiv \frac{\mu'(x_2)}{\mu(x_2)} - \frac{2}{5} [\tanh(L - x_2) - \tanh(x_2)].$$

239 It readily follows that when $\mu(x) > 0$ and $\mu'(x) > 0$, there is always a root to $\mathcal{S} = 0$
 240 with $0 < x_2 < L/2$. Our bifurcation results shown below are for the quadratic
 241 precursor field $\mu(x) = 1 + bx^2$ with $b \geq 0$, as given in (1.2). For this special choice
 242 of μ , instead of computing $x_2 = x_2(b)$ in (3.6) using Newton iterations, we can solve
 243 $\mathcal{S} = 0$ in (3.6) in the explicit form $b = b(x_2)$, where

$$244 \quad (3.7) \quad b = \frac{[\tanh(L - x_2) - \tanh(x_2)]}{x_2 (5 - x_2 [\tanh(L - x_2) - \tanh(x_2)])}.$$

245 By varying x_2 on $0 < x_2 < L/2$ in (3.7), and keeping only points where $b > 0$,
 246 we obtain a simple parametric representation of the symmetric two-spike equilibrium
 247 solution branch with $x_1 = -x_2$. The common spike heights are given by

$$248 \quad (3.8) \quad H_c \equiv H_{1,2} = \frac{1}{6 [\mu(x_2)]^{3/2}} [\tanh(x_2) + \tanh(L - x_2)].$$

249 The linear stability with respect to the DAE dynamics (2.22) at each value of b on this
 250 symmetric solution branch is obtained from a numerical computation of the matrix
 251 spectrum of the generalized eigenvalue problem (3.2).

252 To parameterize asymmetric two-spike equilibria for the special case $\mu = 1 + bx^2$,
 253 we isolate b from setting $\mathcal{N}_1 = \mathcal{N}_2 = 0$ in (3.4a). By equating the resulting two
 254 expressions for b , we obtain an equation relating x_1 and x_2 , in which we treat s as a
 255 parameter. The remaining equation is $\mathcal{N}_3 = 0$ from (3.4b). In this way, for $s \neq 1$, we
 256 calculate solutions $x_1 = x_1(s)$, $x_2 = x_2(s)$ to the two-component coupled system

$$257 \quad (3.9a) \quad \begin{aligned} & (x_2^2 - x_1^2)(e_1 - d_1 s) \left(e_2 + \frac{d_1}{s} \right) - 5 \left[x_2(e_1 - d_1 s) - x_1 \left(e_2 + \frac{d_1}{s} \right) \right] = 0, \\ & s^2 [\mu(x_2)]^{3/2} (c_1 + d_1 s) - [\mu(x_1)]^{3/2} (d_1 + c_2 s) = 0, \end{aligned}$$

258 in which $\mu(x) = 1 + bx^2$, where b is given by

$$259 \quad (3.9b) \quad b = \frac{d_1 s - e_1}{5x_1 + x_1^2(e_1 - d_1 s)}.$$

260 The spike heights are then obtained from (3.4c) in terms of the parameter s . This re-
 261 formulation of (3.4) gives a convenient approach for parameterizing solution branches
 262 of asymmetric two-spike equilibria in terms of the spike height ratio s . For the finite
 263 domain case $L < \infty$, the coefficients c_1 , c_2 , e_1 , e_2 , and d_1 , are given in (3.5), while
 264 when $L = \infty$, we use $c_1 = c_2 = 2/(1 - e^{-2(x_2 - x_1)})$ and $e_1 = -e_2 = \frac{2}{1 - e^{2(x_2 - x_1)}}$.
 265 Finally, at each point on these solution branches the spectrum of the generalized
 266 eigenvalue problem (3.2) is computed to determine the linear stability of asymmetric
 267 spike equilibria to the small eigenvalues.

268 Although this approach works well for moderate values of s , for either very large
 269 or small values of s the nonlinear algebraic system (3.9) is rather poorly conditioned.
 270 As a result we need an alternative approach to compute two-spike equilibria.

271 **3.1. Two-Spike Equilibria: An Alternative Parameterization.** An alter-
 272 native approach to parameterize symmetric and asymmetric two-spike equilibrium
 273 solution branches for the special case where $\mu(x)$ is even is described in Appendix A.
 274 This approach leads to a nonlinear algebraic system in terms of r_+ , r_- , and ℓ , where
 275 ℓ is the symmetry point in the interval $-r_- < \ell < r_+$ at which $h_x = 0$. Here $x_2 = r_+$
 276 and $x_1 = -r_-$ are the two steady-state spike locations with spike heights H_{\pm} . As
 277 shown in Appendix A, with this formulation we must solve

$$278 \quad (3.10a) \quad f(r_+, \ell) = 0, \quad f(r_-, -\ell) = 0, \quad \xi(r_+, \ell) - \xi(r_-, -\ell) = 0,$$

279 for r_{\pm} and ℓ , where $f(r, \ell)$ and $\xi(r, \ell)$ are defined by

$$280 \quad (3.10b) \quad f(r, \ell) = \frac{\mu'(r)}{\mu(r)} + \frac{4}{5} \frac{\langle g_x(r, r; \ell) \rangle}{g(r, r; \ell)}, \quad \xi(r, \ell) = \frac{\mu^{-3/2}(r)}{6} \frac{g(\ell, r; \ell)}{g^2(r, r; \ell)},$$

281 where $\langle g_x(r, r; \ell) \rangle$ indicates the average of g_x across $x = r$. Here $g(x, r; \ell)$ is the 1-D
 282 Green's function, with Dirac point r and left domain endpoint ℓ , satisfying

$$283 \quad (3.11) \quad g_{xx} - g = -\delta(x - r), \quad \ell < x < L; \quad g_x = 0 \quad \text{at} \quad x = \ell, L.$$

284 In the infinite domain case, where $L = \infty$, we calculate that

$$285 \quad (3.12) \quad g(r, r; \ell) = \frac{1}{2} \left(1 + e^{2(\ell - r)} \right), \quad g(\ell, r; \ell) = e^{\ell - r}, \quad \langle g_x(r, r; \ell) \rangle = -\frac{1}{2} e^{2(\ell - r)},$$

286 so that (3.10b) becomes

$$287 \quad (3.13) \quad f(r, \ell) = \frac{2br}{1+br^2} - \frac{4}{5(1+e^{2(r-\ell)})}, \quad \xi(r, \ell) = \frac{2(1+br^2)^{-3/2}}{3} \frac{e^{\ell-r}}{(1+e^{2(\ell-r)})^2}.$$

288 The spike heights for the inhibitor are defined in terms of r_{\pm} by

$$289 \quad (3.14) \quad H_{\pm} = \frac{\mu^{-3/2}(r_{\pm})}{6g(r_{\pm}, r_{\pm}; \pm\ell)} = \frac{(1+br_{\pm}^2)^{-3/2}}{3(1+e^{2(\pm\ell-r_{\pm})})}.$$

290 Alternatively, for the finite domain case, we calculate from (3.11) that

$$291 \quad (3.15) \quad \begin{aligned} g(r, r; \ell) &= \frac{\cosh(r-\ell)\cosh(r-L)}{\sinh(L-\ell)}, \quad g(\ell, r; \ell) = \frac{\cosh(r-L)}{\sinh(L-\ell)}, \\ \langle g_x(r, r; \ell) \rangle &= \frac{\sinh(2r-L-\ell)}{2\sinh(L-\ell)}, \end{aligned}$$

292 so that (3.10b) becomes

$$293 \quad (3.16) \quad f(r, \ell) = \frac{2br}{1+br^2} + \frac{2\sinh(2r-L-\ell)}{5\cosh(r-\ell)\cosh(r-L)}, \quad \xi(r, \ell) = \frac{(1+br^2)^{-3/2}\sinh(L-\ell)}{6\cosh^2(r-\ell)\cosh(r-L)}.$$

294 For this finite domain case, the spike heights are given by

$$295 \quad (3.17) \quad H_{\pm} = -\frac{(1+br_{\pm}^2)^{-3/2}\sinh(\pm\ell-L)}{6\cosh(\pm\ell-r_{\pm})\cosh(r_{\pm}-L)}.$$

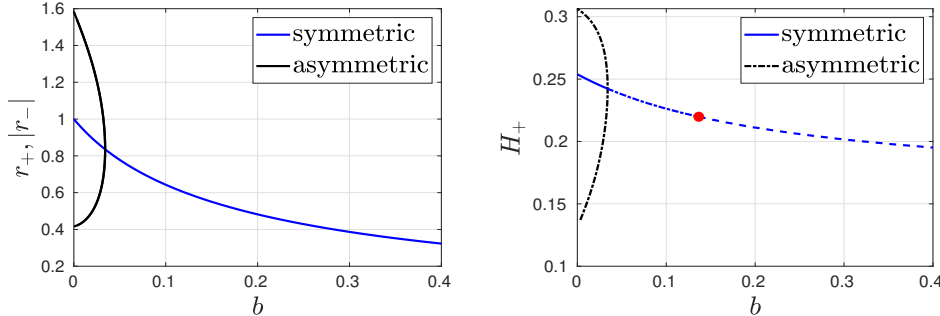


Fig. 3: Left: steady-state spike locations r_+ and $-r_-$ for $L = 2$ versus b in (1.2). Right: height H_+ of the rightmost spike versus b . Solid lines: linearly stable to both the small eigenvalues and the large (NLEP) eigenvalues when $\tau \ll 1$. Dash-dotted lines: unstable for the small eigenvalues but stable for the large eigenvalues when $\tau \ll 1$. Dashed line: stable to the small eigenvalues but unstable to the large eigenvalues when $\tau \ll 1$. Red dot: zero-eigenvalue crossing of the NLEP on the symmetric branch. Bifurcation from symmetric to asymmetric equilibria is subcritical.

296 To compute branches of two-spike equilibria as either b or L is varied, we write
297 (3.10) for r_{\pm} and ℓ in the form $\mathbf{F}(\mathbf{u}, \zeta) = 0$, where

$$298 \quad (3.18) \quad \mathbf{F}(\mathbf{u}, \zeta) \equiv \begin{pmatrix} f(r_+, l) \\ f(r_-, -l) \\ \xi(r_+, l) - \xi(r_-, -l) \end{pmatrix}, \quad \text{with } \mathbf{u} \equiv (r_+, r_-, l)^T, \quad \zeta \equiv (b, L)^T.$$

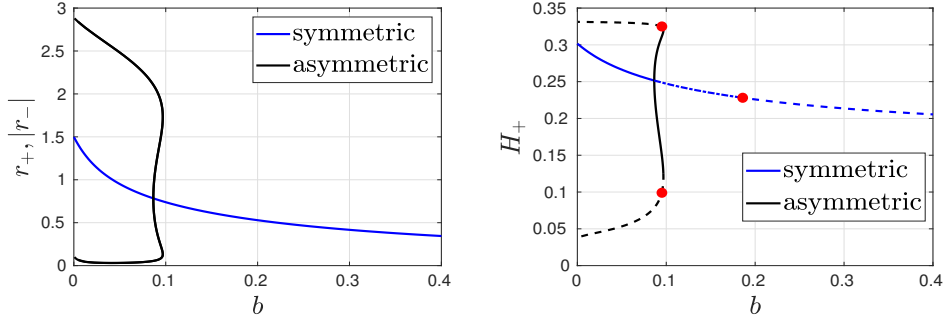


Fig. 4: Similar caption as in Figs. 1 and 3. Left: steady-state spike locations r_+ and $-r_-$ for $L = 3$ versus b . The pitchfork bifurcation is now supercritical. Right: height H_+ of the rightmost spike versus b . Solid lines: linearly stable to both the small eigenvalues and the large (NLEP) eigenvalues when $\tau \ll 1$. Dash-dotted lines: unstable for the small eigenvalues but stable for the large eigenvalues when $\tau \ll 1$. Dashed line: stable to the small eigenvalues but unstable to the large eigenvalues when $\tau \ll 1$. There are only very small (nearly indistinguishable) zones along the asymmetric branches that are unstable to the small eigenvalues. Red dots are where the NLEP has a zero-eigenvalue crossing.

299 Families of solutions and branch points (corresponding to symmetry-breaking
300 pitchfork bifurcations) of this nonlinear system were computed using the two soft-
301 ware packages AUTO (cf. [7]) and COCO (cf. [3]), thereby validating the diagrams
302 provided in Figs. 1, 3, 4, 5, 6 and 7. In Appendix A we give explicit formulas for the
303 Jacobian of \mathbf{F} with respect to \mathbf{u} and the parameter vector ζ , since providing analyt-
304 ical Jacobians significantly improves the performance and accuracy of continuation
305 routines as opposed to using numerical Jacobians based on centered differences.

306 **3.2. Numerical Bifurcation Results for Two-Spike Equilibria.** For $L = 2$,
307 in the left panel of Fig. 3 we plot the numerically computed steady-state spike loca-
308 tions versus the precursor parameter b . In the right panel of Fig. 3, we plot the
309 corresponding height H_+ of the rightmost steady-state spike versus b . In addition,
310 in our plot of H_+ versus b we indicate by various line shadings the linear stability
311 properties of the steady-state solutions. We first observe that asymmetric two-spike
312 equilibria emerge from a subcritical symmetry-breaking bifurcation from the branch
313 of symmetric two-spike equilibria at the critical value $b \approx 0.034$. However, the asym-
314 metric solution branches are all unstable with regards to the small eigenvalues, as
315 indicated by the dash-dotted black curves in the right panel of Fig. 3. Below in the
316 left panel of Fig. 9 we show from a numerical computation of a vector-valued NLEP
317 that these asymmetric branches are all stable on an $\mathcal{O}(1)$ time-scale when τ is suf-
318 ficiently small. These linear stability properties are qualitatively similar to that for
319 two-spike equilibria of the GM model with no precursor field (cf. [29]).

320 In the left and right panels of Fig. 4 and Fig. 1 we plot similar global bifurcation
321 results for two-spike equilibria when $L = 3$ and $L = 5$, respectively. For these values
322 of L , we observe that the symmetry-breaking bifurcation is now supercritical and that
323 a large portion of the bifurcating asymmetric two-spike branch of equilibria is linearly
324 stable with regards to the small eigenvalues. Moreover, as shown below in the middle

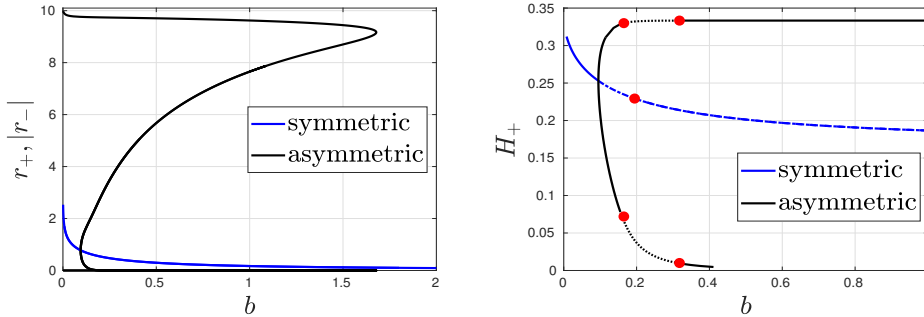


Fig. 5: Left: steady-state spike locations r_+ and $-r_-$ for $L = 10$ versus b . Right: height H_+ of the rightmost spike versus b . Solid lines: linearly stable to both the small eigenvalues and the large (NLEP) eigenvalues when $\tau \ll 1$. Dash-dotted lines: unstable for the small eigenvalues but stable for the large eigenvalues when $\tau \ll 1$. Dashed line: stable to the small eigenvalues but unstable to the large eigenvalues when $\tau \ll 1$. Dotted line: unstable to both the small and large eigenvalues when $\tau \ll 1$. Red dots are where the NLEP has a zero-eigenvalue crossing. In the right panel we have not shown the hairpin turn that occurs when $b \approx 1.67$ that provides the connection between an interior spike and a boundary spike solution.

325 and right panels of Fig. 9, these asymmetric solution branches are all linearly stable
 326 for τ sufficiently small with regards to the large eigenvalues for the range of values
 327 of H_+ between the two red dots shown in the right panel of Fig. 4 for $L = 3$ and of
 328 Fig. 1 for $L = 5$. Overall, this establishes a parameter regime where linearly stable
 329 asymmetric two-spike equilibria occur. For $L = 3$, this theoretical prediction of stable
 330 asymmetric two-spike equilibria is confirmed below in Fig. 12 of §5 from full PDE
 331 simulations of (1.1). For $L = 5$, a similar validation of the linear stability theory
 332 through full PDE simulations was given in Fig. 2 of §1.

333 In Fig. 5 we plot global bifurcation results for two-spike equilibria when $L = 10$.
 334 The right panel of Fig. 5 shows a parameter regime where stable asymmetric two-
 335 spike equilibria can occur when $\tau \ll 1$. However, in contrast to the global bifurcation
 336 diagrams when $L = 2, 3, 5$, we observe that when $L = 10$ there are two zero-crossings
 337 for the NLEP on each asymmetric solution branch, with the pattern being unstable
 338 to both the small and large eigenvalues for some intermediate range of b . This linear
 339 stability behavior with respect to the large eigenvalues is confirmed below in the
 340 left panel of Fig. 10 through numerical computations of the spectrum of a vector-
 341 valued NLEP. Moreover, we observe from Fig. 5 that asymmetric patterns originating
 342 from a symmetry-breaking bifurcation of symmetric two-spike equilibria are path-
 343 connected through a saddle-node point of high curvature to an unstable two-spike
 344 steady-state consisting of a boundary spike of large amplitude and an interior spike
 345 of small amplitude.

346 Similar results are shown in Fig. 6 for the infinite line problem where $L = \infty$. For
 347 this case, stable asymmetric patterns occur near the symmetry-breaking bifurcation
 348 point. Moreover, as for the case where $L = 10$, along the asymmetric solution branch
 349 there is an intermediate range of b where the pattern is unstable to both the small
 350 and large eigenvalues. This instability range of b for the large eigenvalues is observed

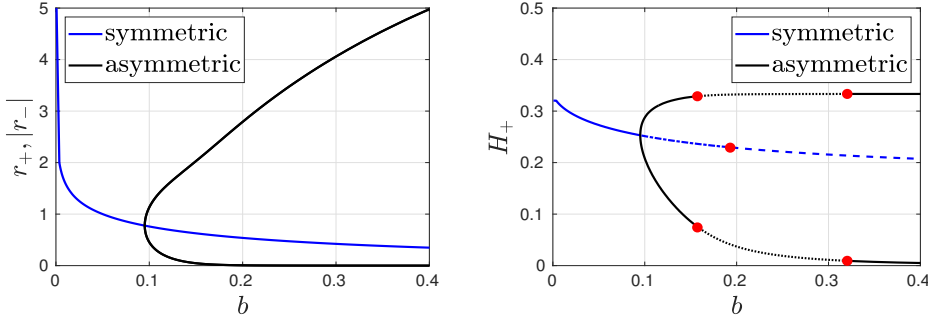


Fig. 6: Left: steady-state spike locations r_+ and $-r_-$ for $L = \infty$ versus b . Right: height H_+ of the rightmost spike versus b . Solid lines: linearly stable to both the small eigenvalues and the large (NLEP) eigenvalues when $\tau \ll 1$. Dash-dotted lines: unstable for the small eigenvalues but stable for the large eigenvalues when $\tau \ll 1$. Dashed line: stable to the small eigenvalues but unstable to the large eigenvalues when $\tau \ll 1$. Dotted line: unstable to both the small and large eigenvalues when $\tau \ll 1$. Red dots are where the NLEP has a zero-eigenvalue crossing. Observe that there is an intermediate range of b along the asymmetric branches where the pattern is unstable to both the small and large eigenvalues. The asymmetric patterns re-stabilize for larger b and results in a spike of large amplitude and another of negligible amplitude.

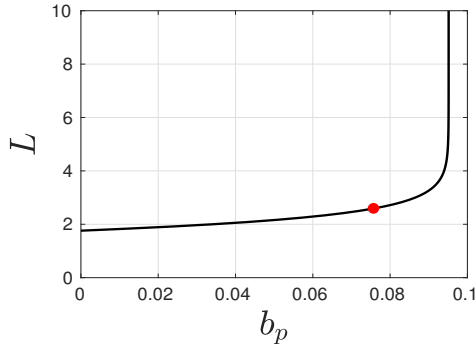


Fig. 7: Symmetry-breaking bifurcation point b_p versus L where the asymmetric branches of two-spike equilibria bifurcate from the symmetric branch. The red dot indicates the critical values $b_c \approx 0.0760$, $L_c \approx 2.597$, $r_{\pm,c} \approx 0.793$ where this bifurcation switches between subcritical and supercritical. The bifurcation curve has a vertical asymptote $b \approx 0.095$ as $L \rightarrow \infty$.

351 in Fig. 10 below from our computations of the spectra of the vector-valued NLEP.
 352 However, when $L = \infty$, there is no boundary spike solution and, as observed in Fig. 6,
 353 the asymmetric solution branch no longer terminates at a finite value of b .

354 **3.3. Computation of a Degenerate Bifurcation Point.** From the global
 355 bifurcation diagrams in Fig. 3 and Fig. 4 we observe that the symmetry-breaking
 356 bifurcation switches from subcritical to supercritical on the range $2 < L < 3$. We now

357 describe a procedure to accurately compute the critical precursor parameter $b = b_c$
 358 and critical domain half-length $L = L_c$ where this switch occurs. The significance
 359 of these critical values is that for $L > L_c$ the asymmetric solution branch is linearly
 360 stable with regards to the small eigenvalues near the bifurcation point.

361 To formulate our procedure for computing these critical values we first define

362 (3.19)
$$W(\ell) \equiv \xi(r_+(\ell), \ell) - \xi(r_-(\ell), -\ell),$$

363 where $r_{\pm} = r_{\pm}(\ell)$ satisfy

364
$$f(r_{\pm}, \pm\ell) = 0.$$

365 Here $\xi(r, \ell)$ and $f(r, \ell)$ are defined in (3.10b). The asymmetric branch corresponds to a
 366 non-zero root of $W(\ell)$ and the symmetry-breaking bifurcation occurs when $W'(0) = 0$.
 367 To compute this point, denote $r = r_{\pm}(0)$, that is, the location of a symmetric spike
 368 which satisfies $f(r, 0) = 0$. Upon differentiating (3.19) implicitly and evaluating at
 369 $\ell = 0$ we obtain that $r'_-(0) = -r'_+(0) = -r'$, so that the bifurcation occurs when the
 370 following system is satisfied:

371 (3.20)
$$\ell = 0, \quad f = 0; \quad r' = -\frac{f_{\ell}}{f_r}; \quad \xi_r r' + \xi_{\ell} = 0.$$

372 In the left panel of Fig. 14 of Appendix A we include the Maple code that computes
 373 this bifurcation point. For example, when $L = 2$ we obtain from solving (3.20) that
 374 $b = 0.03406$ and $r = 0.835585$.

375 Since $W(\ell)$ is an odd function we have for small ℓ that

376
$$W(\ell) \sim \ell W'(0) + \ell^3 \frac{W'''(0)}{6} + O(\ell^5),$$

377 with all even derivatives of W being zero. The criticality of the bifurcation depends on
 378 the sign of $W'''(0)$. A positive sign corresponds to a supercritical bifurcation, whereas
 379 a negative sign corresponds to a subcritical bifurcation. The change of bifurcation
 380 occurs when $W'''(0) = W'(0) = 0$. To compute $W'''(0)$, we differentiate implicitly
 381 and set $\ell = 0$. We readily calculate that

382
$$W'(0) = \xi_r r' + \xi_{\ell}, \quad W''(0) = \xi_{rr} r'^2 + 2\xi_{r\ell} r' + \xi_r r'' + \xi_{\ell\ell},$$

 383
$$W'''(0) = \xi_{rrr} r'^3 + 3\xi_{rr\ell} r'^2 + 3\xi_{r\ell\ell} r' + 3\xi_{rr} r' r'' + 3\xi_{r\ell} r'' + \xi_r r''' + \xi_{\ell\ell\ell}.$$

385 The values of r , r' and r'' are obtained by differentiating f implicitly. This yields

386
$$r' = -\frac{f_{\ell}}{f_r}, \quad r'' = -\frac{f_{rr} r'^2 + 2f_{r\ell} r' + f_{\ell\ell}}{f_r},$$

 387
$$r''' = -\frac{f_{rrr} r'^3 + 3f_{rr\ell} r'^2 + 3f_{r\ell\ell} r' + 3f_{rr} r' r'' + 3f_{r\ell} r'' + f_{\ell\ell\ell}}{f_r},$$

389 which are then evaluated at $\ell = 0$. In this way, the set of equations

390 (3.21)
$$\ell = 0, \quad f = 0; \quad W'(0) = 0, \quad W'''(0) = 0,$$

391 must be solved numerically to obtain the higher-order bifurcation point. The right
 392 panel of Fig. 14 of Appendix A shows the Maple implementation. Although the system

393 (3.21) is very large (its length is about 20,000 bytes in Maple), its numerical solution
 394 is found instantaneously, yielding

395 (3.22) $L = L_c \equiv 2.5972, b = b_c \equiv 0.07596, r = r_c \equiv .792655.$

396 We conclude that the symmetry-breaking bifurcation is supercritical when $L > 2.5972$
 397 and is subcritical when $L < 2.5972$.

398 **4. NLEP Stability Analysis.** We now examine the stability on an $\mathcal{O}(1)$ time-
 399 scale of steady-state spike equilibria of (1.1), labeled by a_e and h_e . We will derive
 400 a new vector-valued nonlocal eigenvalue problem governing instabilities of the spike
 401 amplitudes on an $\mathcal{O}(1)$ time-scale. From this vector-NLEP, we will analyze in de-
 402 tail the linear stability of the two-spike equilibria constructed in §3 to these “large
 403 eigenvalues” for the choice $\mu = 1 + bx^2$.

404 To formulate the linear stability problem, we first introduce the perturbation

405 (4.1) $a(x, t) = a_e + e^{\lambda t} \phi(x), \quad h(x, t) = h_e + e^{\lambda t} \psi(x),$

406 into (1.1) and linearize. This leads to the singularly perturbed eigenvalue problem

407 (4.2a) $\varepsilon^2 \phi_{xx} - \mu(x) \phi + \frac{2a_e}{h_e} \phi - \frac{a_e^2}{h_e^2} \psi = \lambda \phi, \quad |x| \leq L; \quad \phi_x(\pm L) = 0,$

408 (4.2b) $\psi_{xx} - (1 + \tau \lambda) \psi = -\frac{2}{\varepsilon} a_e \phi, \quad |x| \leq L; \quad \psi_x(\pm L) = 0.$

410
 411 In the inner region near a spike at $x = x_j$, we have from (2.4) that

412 $a_e \sim \mu_j H_j w(\sqrt{\mu_j} y_j) \quad h_e \sim H_j, \quad \text{where } y_j = \varepsilon^{-1}(x - x_j),$

413 $\mu_j \equiv \mu(x_j)$, and $w(z) = \frac{3}{2} \operatorname{sech}^2(z/2)$. Here H_j is the spike height obtained from the
 414 steady-state of (2.22). Next, we introduce the localized eigenfunction

415 (4.3) $\Phi_j(y_j) = \phi(x_j + \varepsilon y_j),$

416 and obtain from (4.2a) that on $-\infty < y_j < \infty$, and for each $j = 1, \dots, N$,

417 (4.4) $\frac{d^2 \Phi_j}{dy_j^2} - \mu_j \Phi_j + 2\mu_j w(\sqrt{\mu_j} y_j) \Phi_j - \mu_j^2 [w(\sqrt{\mu_j} y_j)]^2 \Psi_j = \lambda \Phi_j,$

418 where Ψ_j is a constant to be determined. Then, we let $z \equiv \sqrt{\mu_j} y_j$, and define $\hat{\Phi}_j(z) \equiv$
 419 $\Phi_j(z/\sqrt{\mu_j})$, so that (4.4) becomes

420 (4.5) $\frac{d^2 \hat{\Phi}_j}{dz^2} - \hat{\Phi}_j + 2w(z)\hat{\Phi}_j - \mu_j [w(z)]^2 \Psi_j = \frac{\lambda}{\mu_j} \hat{\Phi}_j, \quad -\infty < z < \infty.$

421 To determine Ψ_j , we must construct the outer solution for ψ in (4.2b). In the
 422 sense of distributions we calculate for $\varepsilon \rightarrow 0$ that

423 (4.6) $\frac{2}{\varepsilon} a_e \phi \rightarrow 2H_j \sqrt{\mu_j} \left(\int_{-\infty}^{\infty} w(z) \hat{\Phi}_j(z) dz \right) \delta(x - x_j).$

424 In this way, we obtain that the outer solution for ψ in (4.2b) satisfies

$$425 \quad (4.7a) \quad \psi_{xx} - \theta_\lambda^2 \psi = -2 \sum_{j=1}^n H_j \sqrt{\mu_j} \left(\int_{-\infty}^{\infty} w(z) \hat{\Phi}_j(z) dz \right) \delta(x - x_j), \quad |x| \leq L,$$

$$426 \quad (4.7b) \quad \psi_x(\pm L) = 0, \quad \theta_\lambda \equiv \sqrt{1 + \tau \lambda}.$$

428 In (4.7b) we must choose the principal branch of θ_λ . The constants Ψ_j for $j = 1, \dots, N$
429 are obtained from the matching condition that $\Psi_j = \psi(x_j)$ for $j = 1, \dots, N$.

430 By solving (4.7) on each subinterval we readily derive a linear algebraic system
431 for $\Psi \equiv (\Psi_1, \dots, \Psi_N)^T$ in the form

$$432 \quad (4.8) \quad \mathcal{B}_\lambda \Psi = \frac{2}{\sqrt{1 + \tau \lambda}} \mathcal{U}^{1/2} \mathcal{H} \left(\int_{-\infty}^{\infty} w \Psi dz \right),$$

433 where the diagonal matrices \mathcal{U} and \mathcal{H} have diagonal entries $(\mathcal{U})_{jj} = \mu(x_j)$ and $(\mathcal{H})_{jj} =$
434 H_j for $j = 1, \dots, N$. In (4.8), \mathcal{B}_λ is defined by

$$435 \quad (4.9a) \quad \mathcal{B}_\lambda = \begin{pmatrix} c_{1\lambda} & d_{1\lambda} & & 0 \\ d_{1\lambda} & \ddots & \ddots & \\ & \ddots & \ddots & d_{N-1\lambda} \\ 0 & & d_{N-1\lambda} & c_{N\lambda} \end{pmatrix},$$

436 where the matrix entries are given by

$$437 \quad (4.9b) \quad \begin{aligned} c_{1\lambda} &= \coth(\theta_\lambda(x_2 - x_1)) + \tanh(\theta_\lambda(L + x_1)), \\ c_{N\lambda} &= \coth(\theta_\lambda(x_N - x_{N-1})) + \tanh(\theta_\lambda(L - x_N)), \\ c_{j\lambda} &= \coth(\theta_\lambda(x_{j+1} - x_j)) + \coth(\theta_\lambda(x_j - x_{j-1})), \quad j = 2, \dots, N-1, \\ d_{j\lambda} &= -\operatorname{csch}(\theta_\lambda(x_{j+1} - x_j)), \quad j = 1, \dots, N-1. \end{aligned}$$

438 Next, upon substituting (4.8) into (4.5), we obtain the following vector-valued
439 NLEP for $\hat{\Phi} \equiv (\hat{\Phi}_1, \dots, \hat{\Phi}_N)^T$ on $-\infty < z < \infty$;
440

$$441 \quad (4.10a) \quad \mathcal{L}\hat{\Phi} - w^2 \frac{\int_{-\infty}^{\infty} w \mathcal{E}_\lambda \hat{\Phi} dz}{\int_{-\infty}^{\infty} w^2 dz} = \lambda \mathcal{U}^{-1} \hat{\Phi}; \quad \hat{\Phi} \rightarrow \mathbf{0} \quad \text{as } |z| \rightarrow \infty,$$

$$442 \quad (4.10b) \quad \mathcal{E}_\lambda \equiv \frac{12}{\sqrt{1 + \tau \lambda}} \mathcal{U} \mathcal{B}_\lambda^{-1} \mathcal{U}^{-1} \left(\mathcal{U}^{3/2} \mathcal{H} \right), \quad \mathcal{L}\hat{\Phi} \equiv \hat{\Phi}'' - \hat{\Phi} + 2w\hat{\Phi}.$$

444 We then diagonalize \mathcal{E}_λ by finding the eigenvalues $\mathcal{E}_\lambda e = \chi_\lambda e$ and obtain that

$$445 \quad (4.11) \quad \mathcal{E}_\lambda = \mathcal{V} \Lambda \mathcal{V}^{-1},$$

446 where \mathcal{V} is the matrix of eigenvectors of \mathcal{E}_λ and Λ is the diagonal matrix of eigenvalues
447 with $(\Lambda)_{jj} = \chi_{\lambda,j}$, for $j = 1, \dots, N$. Then, by defining $\tilde{\Phi} = \mathcal{V}^{-1} \hat{\Phi}$, we obtain the
448 following vector-valued NLEP defined on $-\infty < z < \infty$ with $\tilde{\Phi} \rightarrow 0$ as $|z| \rightarrow \infty$:

$$449 \quad (4.12) \quad \mathcal{L}\tilde{\Phi} - w^2 \Lambda \frac{\int_{-\infty}^{\infty} w \tilde{\Phi} dz}{\int_{-\infty}^{\infty} w^2 dz} = \lambda \mathcal{C} \tilde{\Phi}; \quad \mathcal{C} \equiv \mathcal{V}^{-1} \mathcal{U}^{-1} \mathcal{V}.$$

450 The key difference between this NLEP analysis and that for the Gierer-Meinhardt
 451 model with no precursor field in [15] and [14] is that the NLEP cannot be diagonalized
 452 into N separate scalar NLEPs, one for each eigenvalue of Λ . From (4.12) we observe
 453 that the NLEPs are coupled through the matrix \mathcal{C} .

454 We now study (4.12) for our two-spike symmetric and asymmetric equilibria con-
 455 structed in §3 for $\mu = 1 + bx^2$.

456 **4.1. NLEP Analysis: Symmetric 2-Spike Equilibria.** For the symmetric
 457 two-spike case with $x_2 = -x_1$, we use $\mathcal{U} = \mu(x_2)I$ and $\mathcal{H} = H_c I$, to get from (4.10b)
 458 that

$$(4.13) \quad \mathcal{E}_\lambda = \frac{12}{\sqrt{1 + \tau\lambda}} [\mu(x_2)]^{3/2} H_c \mathcal{B}_\lambda^{-1}, \quad \text{where} \quad [\mu(x_2)]^{3/2} H_c = \tanh(x_2) + \tanh(L - x_2),$$

460 as obtained from (3.8). We readily calculate the matrix spectrum of \mathcal{B}_λ as

$$(4.14) \quad \begin{aligned} \mathcal{B}_\lambda \mathbf{v}_1 &= \kappa_{1\lambda} \mathbf{v}_1; & \mathbf{v}_1 &= (1, 1)^T, & \kappa_{1\lambda} &\equiv \tanh(\theta_\lambda x_2) + \tanh(\theta_\lambda(L - x_2)), \\ \mathcal{B}_\lambda \mathbf{v}_2 &= \kappa_{2\lambda} \mathbf{v}_2; & \mathbf{v}_2 &= (1, -1)^T, & \kappa_{2\lambda} &\equiv \coth(\theta_\lambda x_2) + \tanh(\theta_\lambda(L - x_2)). \end{aligned}$$

462 In this way, for symmetric two-spike equilibria, we obtain that (4.12) is equivalent to
 463 the two scalar NLEPs, with NLEP *multipliers* $\chi_{1,\lambda}$ and $\chi_{2,\lambda}$, defined by

$$(4.15a) \quad \mathcal{L}\tilde{\Phi} - w^2 \Lambda \frac{\int_{-\infty}^{\infty} w \tilde{\Phi} dz}{\int_{-\infty}^{\infty} w^2 dz} = \frac{\lambda}{[\mu(x_2)]^{3/2}} \tilde{\Phi}, \quad -\infty < z < \infty; \quad \tilde{\Phi} \rightarrow 0 \quad \text{as} \quad |z| \rightarrow \infty;$$

$$(4.15b) \quad (\Lambda)_{11} \equiv \chi_{1,\lambda} = \frac{2}{\sqrt{1 + \tau\lambda}} \left(\frac{\tanh(x_2) + \tanh(L - x_2)}{\tanh(\theta_\lambda x_2) + \tanh(\theta_\lambda(L - x_2))} \right),$$

$$(4.15c) \quad (\Lambda)_{22} \equiv \chi_{2,\lambda} = \frac{2}{\sqrt{1 + \tau\lambda}} \left(\frac{\tanh(x_2) + \tanh(L - x_2)}{\coth(\theta_\lambda x_2) + \tanh(\theta_\lambda(L - x_2))} \right),$$

468 where $\theta_\lambda = \sqrt{1 + \tau\lambda}$.

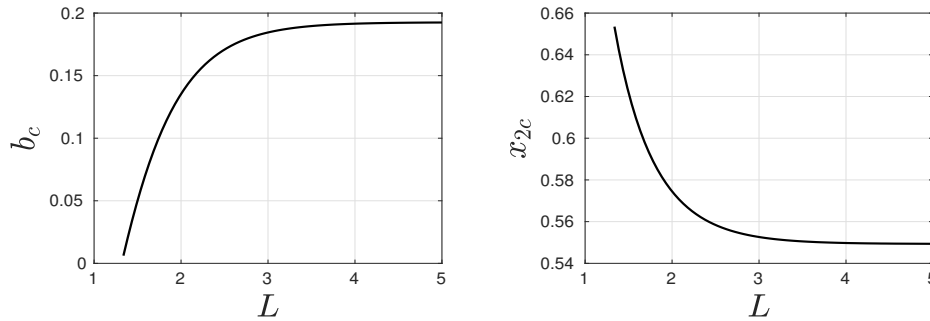


Fig. 8: Critical values b_c of the precursor parameter b (left panel) and the spike location x_{2c} (right panel) versus L where the NLEP (4.15) with multiplier $\chi_{2,\lambda}$ has a zero-eigenvalue crossing for the linearization of a symmetric two-spike steady-state. For $x_2 < x_{2c}$, or equivalently for $b > b_c$, a competition instability on an $\mathcal{O}(1)$ time-scale occurs.

469 We first consider the *competition mode* corresponding to $\mathbf{v}_2 = (1, -1)^T$ where the
 470 multiplier of the NLEP in (4.15a) is $\chi_{2,\lambda}$, which depends on λ through the product
 471 $\tau\lambda$, so that $\chi_{2,\lambda} = \chi_{2,\lambda}(\tau\lambda)$. From Proposition 3.6 of [24], we conclude for this
 472 competition mode that there is a unique eigenvalue in $\text{Re}(\lambda) > 0$ for any $\tau > 0$ when
 473 $\chi_{2,\lambda}(0) < 2$. By using (4.15c), we calculate that $\chi_{2,\lambda}(0) < 2$ when

$$474 \quad 2 \tanh(x_2) + 2 \tanh(L - x_2) < \coth(x_2) + \tanh(L - x_2),$$

475 which, after some algebra, reduces to

$$476 \quad (4.16) \quad \coth(x_2) \coth(L) > 2 \quad \implies \quad 0 < x_2 < x_{2c} \equiv \frac{1}{2} \log \left(\frac{2 + \coth L}{2 - \coth L} \right),$$

477 provided that $L > L_c \equiv \log(2 + \sqrt{3}) \approx 1.3169$. We conclude that a competition
 478 instability occurs whenever spikes become too close. When $L < L_c$, a competition
 479 instability occurs for any $x_2 > 0$. Equivalently, from (3.7), we conclude that on the
 480 range $L > L_c$ a competition instability occurs along the symmetric branch of equilibria
 481 whenever the precursor parameter b satisfies $b > b_c$, where

$$482 \quad (4.17) \quad b_c = \frac{[\tanh(L - x_{2c}) - \tanh(x_{2c})]}{x_{2c} (5 - x_{2c} [\tanh(L - x_{2c}) - \tanh(x_{2c})])}.$$

483 In Fig. 8 we plot b_c and x_{2c} versus L on the range $L > L_c \approx 1.3169$. Numerical
 484 values for b_c for different L correspond to the red dots on the symmetric branches
 485 of equilibria shown in Fig. 1, and in Figs. 3, 4, 5, 6. For $b < b_c$, or equivalently for
 486 $x_2 > x_{2c}$, Proposition 3.6 of [24] can be used to prove that the two-spike symmetric
 487 steady-state is linearly stable on $\mathcal{O}(1)$ time-scales whenever τ in (1.1) is below a Hopf
 488 bifurcation threshold τ_H . We refer the reader to [24] for the proof of this statement.

489 Next, we briefly consider the NLEP (4.15) for the synchronous mode $\mathbf{v}_1 = (1, 1)^T$,
 490 where the NLEP multiplier $\chi_{1,\lambda}$ is given in (4.15b). We calculate that $\chi_{1,\lambda}(0) = 2$,
 491 for any $\tau > 0$ and $b > 0$. As a result, from Theorem 2.4 of [28] (see also [30]) we
 492 conclude that the NLEP for the synchronous mode has no eigenvalues in $\text{Re}(\lambda) > 0$
 493 when $\tau = 0$, or when τ is sufficiently small. As similar to the analysis in [28] with
 494 no precursor, a Hopf bifurcation can occur when τ exceeds a threshold, which now
 495 depends on b and L . We do not calculate this Hopf point numerically here.

496 We summarize our NLEP stability result for the symmetric two-spike steady-state
 497 branch as follows:

498 **PROPOSITION 1.** *Consider the two-spike symmetric steady-state solution for (1.1)
 499 with precursor $\mu(x) = 1 + bx^2$, where the spike locations x_1 and x_2 , with $x_2 = -x_1$ are
 500 given in terms of b by (3.7). Suppose that $L > L_c \equiv \log(2 + \sqrt{3}) \approx 1.3169$ and define
 501 the critical half-distance x_{2c} between the spikes and the critical precursor parameter
 502 b_c by (4.16) and (4.17), respectively. Then, for any b with $b > b_c$, or equivalently
 503 for any x_2 with $x_2 < x_{2c}$, the NLEP (4.15) with multiplier $\chi_{2,\lambda}$ for the competition
 504 mode has a unique unstable eigenvalue in $\text{Re}(\lambda) > 0$. Alternatively, if $b < b_c$, and
 505 for $0 \leq \tau < \tau_H$, the two-spike symmetric steady-state is linearly stable on $\mathcal{O}(1)$ time-
 506 scales to the competition mode. Finally, the NLEP (4.15) for the synchronous mode,
 507 with multiplier $\chi_{1,\lambda}$, has no unstable eigenvalues when $\tau > 0$ is sufficiently small.*

508 **4.2. NLEP Analysis: Asymmetric 2-Spike Equilibria.** We will analyze the
 509 NLEP (4.10) for two-spike asymmetric equilibria for the special case where $\tau = 0$. To

510 do so, we set $\mathcal{F}_3 = \mathcal{F}_4 = 0$ in (3.1) to calculate that

511 (4.18)
$$\mathcal{U}^{3/2}\mathcal{H} = \mathcal{Z}, \quad \text{where} \quad \mathcal{Z} \equiv \frac{1}{6} \begin{pmatrix} c_1 + d_1 s & 0 \\ 0 & c_2 + d_1/s \end{pmatrix},$$

512 with $s = H_2/H_1$. As a result, since \mathcal{U} and \mathcal{Z} are diagonal matrices, we can write the
513 NLEP in (4.10) when $\tau = 0$ as

514 (4.19)
$$\mathcal{L}\hat{\Phi} - w^2 \frac{\int_{-\infty}^{\infty} w\mathcal{E}_{\lambda}\hat{\Phi} dz}{\int_{-\infty}^{\infty} w^2 dz} = \lambda\mathcal{U}^{-1}\hat{\Phi}; \quad \mathcal{E}_{\lambda} \equiv 2\mathcal{U}\mathcal{B}_{\lambda}^{-1}\mathcal{Z}\mathcal{U}^{-1}.$$

515 Next, upon defining \mathcal{A} by $\mathcal{A} = \mathcal{Z}^{-1}\mathcal{B}_{\lambda}$, we calculate its matrix spectrum $\mathcal{A}\mathbf{v} = \kappa\mathbf{v}$,
516 which can be written as $\mathcal{B}_{\lambda}\mathbf{v} = \kappa\mathcal{Z}\mathbf{v}$. By using (4.9) for \mathcal{B}_{λ} with $\tau = 0$, and (4.18)
517 for \mathcal{Z} , we conclude that κ must satisfy

518 (4.20a)
$$\det \begin{pmatrix} c_1 - \kappa(c_1 + d_1 s) & d_1 \\ d_1 & c_2 - \kappa(c_2 + \frac{d_1}{s}) \end{pmatrix} = 0,$$

519 which yields that κ satisfies the quadratic equation

520 (4.20b)
$$\kappa^2 \left(c_1 c_2 + c_2 d_1 s + d_1^2 + \frac{c_1 d_1}{s} \right) - \kappa \left(2c_1 c_2 + d_1 s c_2 + \frac{d_1 c_1}{s} \right) + c_1 c_2 - d_1^2 = 0.$$

521 Observe that $\kappa_1 = 1$ is always an eigenvalue, and so κ_2 can readily be found. A simple
522 calculation yields that the matrix spectrum of $\mathcal{Z}^{-1}\mathcal{B}_{\lambda}$ is

523 (4.21)
$$\begin{aligned} \kappa_1 &= 1, \quad \mathbf{v}_1 = \begin{pmatrix} 1 \\ s \end{pmatrix}, \\ \kappa_2 &= \frac{c_1 c_2 - d_1^2}{c_1 c_2 + d_1^2 + d_1(c_2 s + c_1/s)}, \quad \mathbf{v}_2 = \begin{pmatrix} -d_1 \\ c_1 - \kappa_2(c_1 + d_1 s) \end{pmatrix}. \end{aligned}$$

524 Next, we define the eigenvector matrix \mathcal{V} , the diagonal matrix Λ , and the matrix \mathcal{C}
525 by

(4.22)
$$526 \quad \mathcal{V} \equiv \begin{pmatrix} 1 & -d_1 \\ s & c_1 - \kappa_2(c_1 + d_1 s) \end{pmatrix}, \quad \Lambda \equiv \begin{pmatrix} 2 & 0 \\ 0 & 2/\kappa_2 \end{pmatrix}, \quad \mathcal{C} \equiv \mathcal{V}^{-1}\mathcal{U}^{-1}\mathcal{V},$$

527 so that $\mathcal{E}_{\lambda} = 2\mathcal{U}\mathcal{A}^{-1}\mathcal{U}^{-1} = (\mathcal{U}\mathcal{V})\Lambda(\mathcal{U}\mathcal{V})^{-1}$. Finally, by setting $\tilde{\Phi} = (\mathcal{U}\mathcal{V})^{-1}\hat{\Phi}$, we
528 obtain the vector-valued NLEP (4.12), where Λ and \mathcal{C} are defined explicitly in (4.22).

529 In the context of spike stability, the vector-valued NLEP (4.12) is a new linear
530 stability problem, for which the NLEP stability results for the scalar case in [30], [28],
531 and [4] are not directly applicable. Analytically, it is challenging to provide necessary
532 and sufficient conditions to guarantee that the NLEP (4.12) has no eigenvalues in
533 $\text{Re}(\lambda) > 0$. However, one can analyze any zero-eigenvalue crossings, by using the
534 well-known identity $L_0 w = w^2$. By setting $\tilde{\Phi} = (0, w)^T$, we observe from (4.12)
535 that a zero-eigenvalue crossing will occur when $\kappa_2 = 2$. By using (4.21) for κ_2 , a
536 zero-eigenvalue crossing occurs when

537 (4.23)
$$c_1 c_2 + 3d_1^2 = 2|d_1| \left(c_2 s + \frac{c_1}{s} \right).$$

538 Here c_1 , c_2 and d_1 are determined in terms of the steady-state spike locations x_1
539 and x_2 by (3.5), while $s = H_2/H_1$ parameterizes the branch of asymmetric two-spike
540 equilibria in either (3.4), or equivalently (3.9). An interpretation of the zero-eigenvalue
541 crossing is given in the following remark.

542 Remark 4.1. Equilibria of the DAE system (2.22) are solutions to the nonlinear
 543 algebraic system $\mathcal{F}(x_1, x_2, H_1, H_2) = \mathbf{0}$ for $\mathcal{F} \in \mathbb{R}^4$, as given in (3.1). For a fixed x_1
 544 and x_2 , we claim that the linearization of the subsystem $\mathcal{F}_3 = \mathcal{F}_4 = 0$ in (3.1) for the
 545 spike amplitudes is not invertible when the NLEP has a zero-eigenvalue crossing. To
 546 see this, we calculate along solutions to (3.1) that

$$\begin{aligned} J_3 &\equiv \begin{pmatrix} \mathcal{F}_{3H_1} & \mathcal{F}_{3H_2} \\ \mathcal{F}_{4H_1} & \mathcal{F}_{4H_2} \end{pmatrix} \\ 547 &= \begin{pmatrix} 12\mu_1^{3/2}H_1 - c_1 & -d_1 \\ -d_1 & 12\mu_2^{3/2}H_2 - c_2 \end{pmatrix} = \begin{pmatrix} c_1 + 2d_1s & -d_1 \\ -d_1 & c_2 + 2d_1/s \end{pmatrix}. \end{aligned}$$

548 A simple calculation shows that $\det(J_3) = 0$ if and only if

$$549 \quad (4.24) \quad c_1c_2 + 3d_1^2 = -2d_1 \left(c_2s + \frac{c_1}{s} \right),$$

550 which is the condition derived in (4.23) for the zero-eigenvalue crossing of the NLEP.

551 The condition (4.23) for a zero-eigenvalue crossing is indicated by the red dots on
 552 the asymmetric branches of equilibria shown in Fig. 1, and in Figs. 3, 4, 5, 6. For the
 553 corresponding scalar NLEP case, where \mathcal{C} is a multiple of the identity, the rigorous
 554 results of [30] prove that $\text{Re}(\lambda) \leq 0$ if and only if $\kappa_2 < 2$, and that an unstable real
 555 eigenvalue exists if $\kappa_2 > 2$. We now investigate numerically whether these optimal
 556 linear stability results persist for the vector-valued NLEP.

557 4.2.1. Numerical Computation of the Vector-Valued NLEP.

We compute the discrete eigenvalues of the vector-valued NLEP (4.12) for $\tilde{\Phi} \equiv (\tilde{\Phi}_1, \tilde{\Phi}_2)^T$,
 558 where Λ and \mathcal{C} are defined in (4.22). To do so, we use a second-order centered finite
 559 difference discretization of the NLEP, where the nonlocal term is discretized using the
 560 trapezoidal rule. We discretize (4.12) on $0 \leq z \leq z_M$ using the nodal values

$$\begin{aligned} 562 \quad z_j &= h(j-1), \quad h \equiv \frac{z_M}{n-1}, \quad w_j = w(z_j) = \frac{3}{2} \operatorname{sech}^2 \left(\frac{z_j}{2} \right), \quad j = 1, \dots, n, \\ 563 \quad \Psi &\equiv (\Psi_{1,1}, \dots, \Psi_{1,n}, \Psi_{2,1}, \dots, \Psi_{2,n})^T, \end{aligned}$$

565 where $\Psi_{1,j} \approx \tilde{\Phi}_1(z_j)$ and $\Psi_{2,j} \approx \tilde{\Phi}_2(z_j)$ for $j = 1, \dots, n$. We impose that $\tilde{\Phi}' = 0$ at
 566 $z = 0, z_M$, which is discretized by centered differences. The resulting block-structured
 567 matrix eigenvalue problem for the pair $\Psi \in \mathbb{R}^{2n}$ and λ is given by

$$568 \quad (4.25a) \quad (\mathcal{K}_n + \mathcal{M}_n) \Psi = \lambda \mathcal{P}_n \Psi,$$

569 where the matrices $\mathcal{K}_n \in \mathbb{R}^{2n,2n}$, $\mathcal{M}_n \in \mathbb{R}^{2n,2n}$ and $\mathcal{P}_n \in \mathbb{R}^{2n,2n}$, are defined by

$$570 \quad (4.25b) \quad \mathcal{K}_n \equiv \begin{pmatrix} \mathcal{K} & 0 \\ 0 & \mathcal{K} \end{pmatrix}, \quad \mathcal{M}_n \equiv \begin{pmatrix} \mathcal{M} & 0 \\ 0 & \kappa_2^{-1}\mathcal{M} \end{pmatrix}, \quad \mathcal{P}_n \equiv \begin{pmatrix} c_{11}I & c_{12}I \\ c_{21}I & c_{22}I \end{pmatrix}.$$

571 Here $I \in \mathbb{R}^{n,n}$ is the identity, and c_{ij} for $1 \leq i, j \leq 2$ are the matrix entries of the
 572 2×2 matrix \mathcal{C} defined in (4.22). In (4.25b), the $n \times n$ tridiagonal matrix \mathcal{K} and the
 573 full $n \times n$ matrix \mathcal{M} are defined, respectively, by

$$\begin{aligned} 574 \quad (4.25c) \quad \mathcal{K}_{1,2} &= \mathcal{K}_{n,n-1} = \frac{2}{h^2}, \quad \mathcal{K}_{ii} = -\frac{2}{h^2} - 1 + 2w_i, \quad \text{for } i = 1, \dots, n, \\ &\mathcal{K}_{i,i+1} = \mathcal{K}_{i,i-1} = \frac{1}{h^2}, \quad \text{for } i = 2, \dots, n-1, \end{aligned}$$

575 and

$$576 \quad (4.25d) \quad \mathcal{M} \equiv -\frac{2h}{3} \begin{pmatrix} w_1^2 \left(\frac{w_1}{2}\right) & w_1^2 w_2 & \dots & w_1^2 w_{n-1} & w_1^2 \left(\frac{w_n}{2}\right) \\ \vdots & \vdots & \vdots & \vdots & \vdots \\ \vdots & \vdots & \vdots & \vdots & \vdots \\ w_n^2 \left(\frac{w_1}{2}\right) & w_n^2 w_2 & \dots & w_n^2 w_{n-1} & w_n^2 \left(\frac{w_n}{2}\right) \end{pmatrix}.$$

577

578 For $n = 250$ and $z_M = 15$, the matrix spectrum of (4.25) is computed numerically
 579 using a generalized matrix eigenvalue solver from EISPACK at each point along the
 580 asymmetric solution branches of two-spike equilibria. In Fig. 9 we plot the first two
 581 eigenvalues of (4.25), defined as those with the largest real parts, versus the height H_+
 582 of the rightmost spike for $L = 2, 3, 5$. In terms of H_+ , we recall that the asymmetric
 583 branches of equilibria for these values of L were shown in the right panels of Figs. 3,
 584 4 and 1, respectively. From Fig. 9 we observe that the first two eigenvalues are
 585 real-valued except for a small range of H_+ when $L = 2$, where they form a complex
 586 conjugate pair. These numerical results confirm the zero-eigenvalue crossing condition
 587 (4.23), obtained by setting $\kappa_2 = 2$, as evidenced by the intersection of the heavy-solid
 588 curves and the horizontal blue lines in Fig. 9. However, most importantly, the results
 589 in Fig. 9 establish numerically that the vector-valued NLEP (4.12), which is valid
 590 for $\tau = 0$, has no unstable discrete eigenvalues whenever $\kappa_2 < 2$, and that there is a
 591 unique unstable discrete eigenvalue when $\kappa_2 > 2$. Increasing the number of gridpoints
 592 n or the cutoff z_M did not alter the results to two decimal places of accuracy.

593 For $L = 10$ and for the infinite domain problem with $L = \infty$, in Fig. 10 we
 594 plot the first two eigenvalues of (4.25) versus the precursor parameter b along the
 595 asymmetric solution branches of Fig. 5 and Fig. 6. From Fig. 10 we observe that along
 596 these solution branches the NLEP has two zero-eigenvalue crossings, corresponding
 597 to where $\kappa_2 = 2$, and that the vector NLEP has a unique unstable eigenvalue between
 598 these crossings. This linear stability behavior is encoded in the global bifurcation
 599 diagrams for $L = 10$ and $L = \infty$ shown in the right panels of Fig. 5 and Fig. 6,
 600 respectively.

601 **5. Validation from PDE Simulations.** In this section, we validate our global
 602 bifurcation and linear stability results for the precursor field $\mu(x) = 1 + bx^2$ from time-
 603 dependent PDE simulations of (1.1). In our simulations, we give initial conditions
 604 for (1.1) that correspond to a two-spike quasi-equilibrium solution, where the spike
 605 heights satisfy the constraint in (2.22) for given spike locations x_1 and x_2 at $t = 0$.

606 For $L = 5$ and $b = 0.12$, the results from the PDE simulations shown in Fig. 2
 607 confirm that a quasi-equilibrium two-spike pattern tends to a stable asymmetric two-
 608 spike equilibrium on a long time scale, as predicted by the bifurcation diagram shown
 609 in the right panel of Fig. 1. The other parameter values are shown in caption of Fig. 2.
 610 In contrast, if $b = 0.18$, from the PDE simulation results shown in Fig. 11 we observe
 611 that a two-spike quasi-equilibrium solution undergoes a competition instability leading
 612 to the destruction of a spike. For this parameter set, there is no stable asymmetric
 613 two-spike steady-state pattern as observed from the right panel of Fig. 1.

614 Similarly, for $L = 3$ and $b = 0.09$, we observe from the full numerical results
 615 shown in Fig. 12 that the quasi-equilibrium two-spike pattern converges as t increases
 616 to a stable asymmetric steady-state pattern. As shown in the bifurcation diagram
 617 given in the right panel of Fig. 4 there is a stable asymmetric two-spike steady-state
 618 for these parameter values.

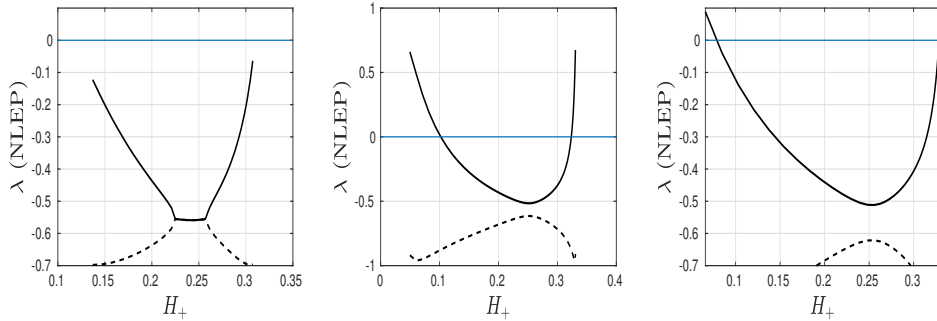


Fig. 9: Plot of the first (heavy solid) and second (dashed) eigenvalues (ordered by the largest real parts), as computed from the discretization of the vector-valued NLEP (4.12) versus the height H_+ of the rightmost spike along the asymmetric solution branches shown in Figs. 3, 4 and 1 for domain half-lengths $L = 2$ (left), $L = 3$ (middle) and $L = 5$ (right), respectively. Numerical evidence shows that when $\kappa_2 < 2$, the vector NLEP has no unstable eigenvalues, and that a unique positive eigenvalue occurs when $\kappa_2 > 2$. Here κ_2 is defined in (4.21) and the zero-eigenvalue crossing occurs when $\kappa_2 = 2$, leading to (4.23). The thin horizontal blue line is the zero-eigenvalue crossing.

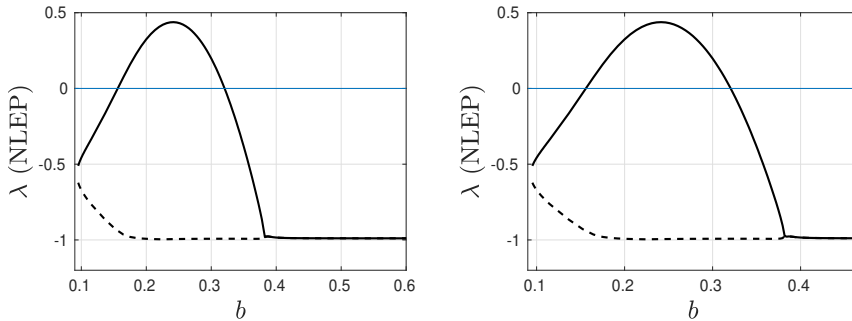


Fig. 10: Plot of the first (heavy solid) and second (dashed) eigenvalues (ordered by the largest real parts), as computed from the discretization of the vector-valued NLEP (4.12) versus the precursor parameter b along the asymmetric solution branches shown in Figs. 5 and 6 for a domain half-length $L = 10$ (left panel) and an infinite domain $L = \infty$ (right panel), respectively. The NLEP has two zero-eigenvalue crossings (intersection with the horizontal blue line) on each portion of the asymmetric branch at parameter values where $\kappa_2 = 2$ (see Fig. 5 and Fig. 6). Between the zero-eigenvalue crossings the vector NLEP has a unique unstable real eigenvalue.

Finally, for $L = 10$, in Fig. 13 we show results for two-spike solutions computed from PDE simulations of (1.1) for $b = 0.15$ and for $b = 0.20$. In the left panel of Fig. 13 we show a stable asymmetric two-spike steady-state for $b = 0.15$ as computed numerically from (1.1), starting from an initial condition chosen to be close to the stable asymmetric pattern predicted from the global bifurcation diagram in Fig. 5.

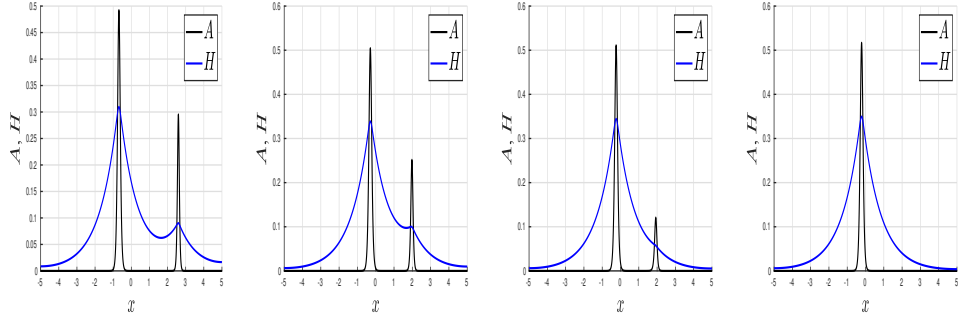


Fig. 11: Time-dependent PDE simulations of (1.1) with $L = 5$, $\varepsilon = 0.05$, and $\tau = 0.25$ for a precursor $\mu(x) = 1 + bx^2$ with $b = 0.18$. Initial condition is a quasi-equilibrium two-spike solution with spike locations $x_1(0) = -1$ and $x_2(0) = 3$. Plots of A and H versus x at four different times showing that one spike is annihilated as time increases. For $b = 0.18$, the right panel in Fig. 1 shows that there is no stable asymmetric two-spike pattern. Left: $t = 180$. Left Middle: $t = 335$. Right Middle: $t = 650$. Right: $t = 800$.

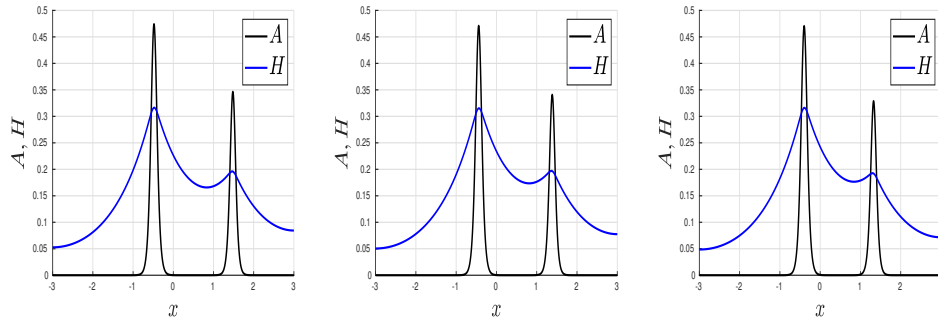


Fig. 12: Time-dependent PDE simulations of (1.1) with $L = 3$, $\varepsilon = 0.05$, and $\tau = 0.15$ for a precursor $\mu(x) = 1 + bx^2$ with $b = 0.09$. Initial condition is a quasi-equilibrium two-spike solution with spike locations $x_1(0) = -0.5$ and $x_2(0) = 1.5$. Plots of A and H versus x at three different times showing the convergence towards a stable asymmetric two-spike pattern as predicted from the right panel of Fig. 4. Left: $t = 31$. Middle: $t = 301$. Right: $t = 900$. As t increases there is only a slight adjustment of the pattern.

624 For $b = 0.20$, where no such stable asymmetric pattern exists from Fig. 5, the PDE
 625 simulations shown in the other three panels in Fig. 13 confirm the instability and
 626 show the annihilation of the small spike as time increases.

627 **6. Discussion.** For the GM model (1.1) with a precursor field $\mu(x) = 1 + bx^2$,
 628 we have shown that a linearly stable asymmetric two-spike steady-state pattern can
 629 emerge from a supercritical pitchfork bifurcation at some critical value of b along a
 630 symmetric branch of two-spike equilibria. For this symmetry-breaking bifurcation, the
 631 critical value of b depends on the domain half-length L . From a linearization around

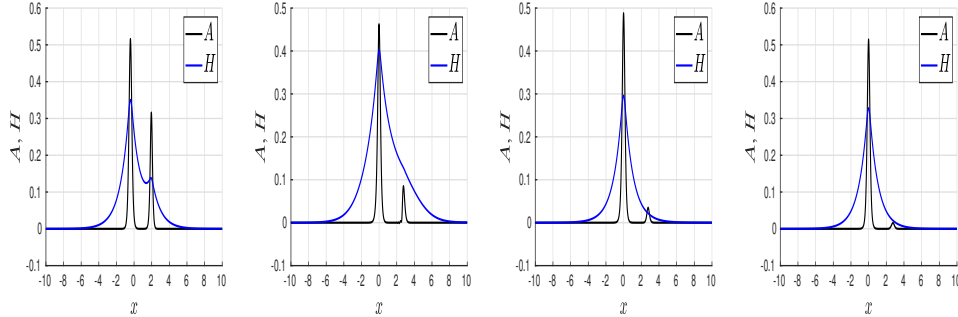


Fig. 13: Left panel: steady-state of time-dependent PDE simulations of (1.1) with $L = 10$, $\varepsilon = 0.10$, and $\tau = 0.15$ for $\mu(x) = 1 + bx^2$ with $b = 0.15$. Other panels: PDE simulations of (1.1) when b is increased to $b = 0.20$ (other parameters the same). For $b = 0.20$, the NLEP stability theory in Fig. 10 predicts no stable asymmetric two-spike steady-state. The PDE numerical results show a collapse of the small spike. Left middle: $t = 0$. Right middle: $t = 0.61$. Right: $t = 1.2$. For the PDE simulations with $b = 0.15$ and $b = 0.20$, the initial condition was a 2% perturbation of the asymmetric steady state shown in the global bifurcation diagram Fig. 5.

632 the steady-state of a DAE system of ODEs for the spike locations and spike heights, we
 633 have shown numerically that some portions of the asymmetric branches of equilibria
 634 are linearly stable to the small eigenvalues. Moreover, from a combined analytical
 635 and numerical investigation of the spectrum of a novel class of vector-valued NLEP,
 636 we have shown that portions of the branches of asymmetric two-spike equilibria are
 637 linearly stable to $\mathcal{O}(1)$ time-scale spike amplitude instabilities. Overall, our combined
 638 analytical and numerical study establishes the qualitatively novel result that linearly
 639 stable asymmetric two-spike equilibria can occur for the GM model with a precursor
 640 field. Asymmetric two-spike equilibria in 1-D for the GM model are all unstable in
 641 the absence of a precursor field [29].

642 Although we have only exhibited stable asymmetric patterns for the GM model
 643 with a specific precursor field with two spikes, the analytical framework we have
 644 employed applies to multiple spikes, to other precursor fields, and to other singularly
 645 perturbed RD systems. In particular, the equilibria of the DAE system (2.18) could be
 646 used to compute the bifurcation diagram of symmetric and asymmetric spike equilibria
 647 for more than two spikes.

648 There are two open directions that warrant further investigation. One specific
 649 focus would be to extend NLEP stability theory for scalar NLEPs to establish an-
 650 alytically necessary and sufficient conditions for the vector-valued NLEP (4.12) to
 651 admit no eigenvalues in $\text{Re}(\lambda) > 0$. In this NLEP we would allow \mathcal{C} in (4.12) to be
 652 an arbitrary matrix with positive eigenvalues. A second open direction would be to
 653 extend the 1-D theory for the GM model with a precursor field to a 2-D setting in
 654 order to construct stable asymmetric spot patterns in a 2-D domain.

655 **7. Acknowledgements.** Theodore Kolokolnikov and Michael Ward were sup-
 656 ported by NSERC Discovery grants. Frédéric Paquin-Lefebvre was supported by a
 657 UBC Four-Year Graduate Fellowship.

658 **Appendix A. Alternative Formulation of Two-Spike Equilibria.**

659 In this appendix we briefly outline the derivation of the coupled system (3.10)
 660 characterizing two-spike equilibria for the special case where $\mu(x)$ is even in x . We
 661 center the spikes at $x_2 = r_+$ and $x_1 = -r_-$, and we let ℓ be the unknown location, with
 662 $x_1 < \ell < x_2$, where $h_x(\ell) = a_x(\ell) = 0$. We label the spike heights as $H_{\pm} = h(\pm r_{\pm})$.

663 To proceed, we first construct a steady-state spike at $x = r_+$ on the interval
 664 (ℓ, L) with $h_x = 0$ and $a_x = 0$ at $x = \ell, L$. A similar construction is made for the
 665 interval $(-L, \ell)$ with a spike at $x = -r_-$. Then, since $\mu(x)$ is even, we can write the
 666 two steady-state conditions in a compact unified form, with the remaining equation
 667 resulting from adjusting $h(\ell)$ so that $h(x)$ is continuous across $x = \ell$.

668 For the right interval $\ell < x < L$ with a spike at $x = r_+$, we proceed as in the
 669 derivation of (2.16) to obtain that r_+ satisfies

$$670 \quad (A.1) \quad -\frac{\mu'(r_+)}{\mu(r_+)} - \frac{4}{5} \frac{\langle g_{1x} \rangle|_{x=r_+}}{g_1|_{x=r_+}} = 0,$$

671 where $\langle g_{1x} \rangle$ is the average of g_{1x} across $x = r_+$. Here $g_1(x, r_+)$ is the 1-D Green's
 672 function satisfying

$$673 \quad (A.2) \quad g_{1xx} - g_1 = -\delta(x - r_+), \quad \ell < x < L; \quad g_{1x} = 0 \quad \text{at } x = \ell, L.$$

674 The inhibitor field $h(x)$ and the spike height $H_+ = h(r_+)$ are given by

$$675 \quad (A.3) \quad h(x) = 6H_+^2 \mu_+^{3/2} g_1(x, r_+), \quad H_+ = \frac{\mu_+^{-3/2}}{6g_1|_{x=r_+}},$$

676 where $\mu_+ \equiv \mu(r_+)$. Similarly, for the left interval $-L < x < \ell$ with a spike at
 677 $x = -r_-$, we obtain that r_- satisfies

$$678 \quad (A.4) \quad -\frac{\mu'(-r_-)}{\mu(-r_-)} - \frac{4}{5} \frac{\langle g_{2x} \rangle|_{x=-r_-}}{g_2|_{x=-r_-}} = 0,$$

679 where $g_2(x, r_-)$ satisfies

$$680 \quad (A.5) \quad g_{2xx} - g_2 = -\delta(x + r_-), \quad -L < x < \ell; \quad g_{2x} = 0 \quad \text{at } x = \ell, -L.$$

681 The inhibitor field $h(x)$ and the spike height $H_- = h(-r_-)$ are given by

$$682 \quad (A.6) \quad h(x) = 6H_-^2 \mu_-^{3/2} g_2(x, r_-), \quad H_- = \frac{\mu_-^{-3/2}}{6g_2|_{x=-r_-}},$$

683 where $\mu_- = \mu(-r_-)$.

684 Since $\mu(x)$ is even, we have $\mu(-r_-) = \mu(r_-)$ and $\mu'(-r_-) = -\mu'(r_-)$. Next, we
 685 set $\tilde{x} = -x$ in (A.5) and label $\tilde{g}_2(\tilde{x}, r_-) \equiv g_2(-\tilde{x}, r_-)$, so that (A.4) becomes

$$686 \quad (A.7) \quad -\frac{\mu'(r_-)}{\mu(r_-)} - \frac{4}{5} \frac{\langle \tilde{g}_{2\tilde{x}} \rangle|_{\tilde{x}=r_-}}{\tilde{g}_2|_{\tilde{x}=r_-}} = 0,$$

687 where $\tilde{g}_2(\tilde{x}, r_-)$ satisfies

$$688 \quad (A.8) \quad \tilde{g}_{2\tilde{x}\tilde{x}} - \tilde{g}_2 = -\delta(\tilde{x} - r_-), \quad -\ell < \tilde{x} < L; \quad g_{2\tilde{x}} = 0 \quad \text{at } \tilde{x} = -\ell, L.$$

689 To combine (A.1) and (A.7) into a unified expression it is convenient to define
 690 $g(x, r; \ell)$ as in (3.11), so that $g_1(x, r_+) = g(x, r_+; \ell)$ and $\tilde{g}_2(x, r_-) = g(x, r_-; -\ell)$. In

691 this way, (A.1) and (A.7) reduce to $f(r_+, \ell) = 0$ and $f(r_-, -\ell) = 0$, where $f(r, \ell)$ is
 692 defined in (3.10b). The condition that the inhibitor field is continuous across $x = \ell$,
 693 as obtained by equating the two expressions for $h(\ell)$ in (A.3) and (A.6), yields the
 694 continuity condition $\xi(r_+, \ell) = \xi(r_-, -\ell)$ as written in (3.10b).

695 The computation of two-spike equilibria reduces to finding roots of $\mathbf{F}(\mathbf{u}, \zeta) = 0$,
 696 as defined in (3.18) as the parameter vector $\zeta \equiv (b, L)^T$ is varied. To compute paths
 697 of solutions we employ the software packages AUTO (cf. [7]) and coco (cf. [3]) and
 698 provide the Jacobian matrices

$$699 \quad (A.9) \quad D_u \mathbf{F} = \begin{pmatrix} \frac{\partial f}{\partial r}(r_+, \ell) & 0 & \frac{\partial f}{\partial l}(r_+, \ell) \\ 0 & \frac{\partial f}{\partial r}(r_-, -\ell) & -\frac{\partial f}{\partial l}(r_-, \ell) \\ \frac{\partial \xi}{\partial r}(r_+, \ell) & -\frac{\partial \xi}{\partial r}(r_-, -\ell) & \frac{\partial \xi}{\partial l}(r_+, \ell) + \frac{\partial \xi}{\partial l}(r_-, -\ell) \end{pmatrix},$$

$$700 \quad (A.10) \quad D_\zeta \mathbf{F} = \begin{pmatrix} \frac{\partial f}{\partial b}(r_+, \ell) & \frac{\partial f}{\partial L}(r_+, \ell) \\ \frac{\partial f}{\partial b}(r_-, -\ell) & \frac{\partial f}{\partial L}(r_-, -\ell) \\ \frac{\partial \xi}{\partial b}(r_+, \ell) - \frac{\partial \xi}{\partial b}(r_-, -\ell) & \frac{\partial \xi}{\partial b}(r_+, \ell) - \frac{\partial \xi}{\partial b}(r_-, -\ell) \end{pmatrix}$$

702 By using (3.16) for f and ξ , we can calculate the entries in the Jacobians analytically
 703 as

$$704 \quad (A.11) \quad \begin{aligned} \frac{\partial f}{\partial r} &= \left[\frac{4 \cosh(2r - \ell - L) - 2(\tanh(r - \ell) + \tanh(r - L)) \sinh(2r - \ell - L)}{5 \cosh(r - L) \cosh(r - \ell)} \right] \\ &\quad + \frac{2b(1 - br^2)}{(1 + br^2)^2} \\ \frac{\partial f}{\partial \ell} &= \frac{2}{5} \left[\frac{\sinh(2r - \ell - L) \tanh(r - \ell) - \cosh(2r - \ell - L)}{\cosh(r - L) \cosh(r - \ell)} \right], \\ \frac{\partial f}{\partial b} &= \frac{2r}{(1 + br^2)^2}, \\ \frac{\partial f}{\partial L} &= \frac{2}{5} \left[\frac{\sinh(2r - \ell - L) \tanh(r - L) - \cosh(2r - \ell - L)}{\cosh(r - L) \cosh(r - \ell)} \right], \\ \frac{\partial \xi}{\partial r} &= \frac{\sinh(\ell - L)}{6(1 + br^2)^{5/2}} \left[\frac{3br + (1 + br^2)(2 \tanh(r - \ell) + \tanh(r - L))}{\cosh^2(r - \ell) \cosh(r - L)} \right], \\ \frac{\partial \xi}{\partial \ell} &= \frac{(1 + br^2)^{-3/2}}{6} \left[\frac{2 \tanh(r - \ell) \sinh(L - \ell) - \cosh(L - l)}{\cosh^2(r - \ell) \cosh(r - L)} \right], \\ \frac{\partial \xi}{\partial b} &= -\frac{r^2(1 + br^2)^{-5/2}}{4} \left[\frac{\sinh(L - \ell)}{\cosh^2(r - \ell) \cosh(r - L)} \right], \\ \frac{\partial \xi}{\partial L} &= \frac{(1 + br^2)^{-3/2}}{6} \left[\frac{\cosh(L - \ell) + \sinh(L - \ell) \tanh(r - L)}{\cosh^2(r - \ell) \cosh(r - L)} \right]. \end{aligned}$$

705 Finally, in Fig. 14 we include the Maple code used to compute the symmetry-
 706 breaking bifurcation point as well as parameter set where this bifurcation switches
 707 from subcritical to supercritical. This was described in (3.20) and (3.21) of §3.3.

- 709 [1] V. Brena-Medina, A. Champneys, C. Grierson, M. J. Ward, *Mathematical modeling of plant*
 710 *root hair initiation: dynamics of localized patches*, SIAM J. Appl. Dyn. Sys., **13**(1), (2014),
 711 pp. 210–248.

```

> restart;
> rp := -f1/fr;
Wp := xir*xrp*xil;

> f := 2*b*r/(1+b*r^2)+2*sinh(2*r-L-1)/5*cosh(r-1)/cosh(r-L);
f :=  $\frac{2 b r}{b r^2 + 1} - \frac{2 \sinh(-2 r + L + 1)}{5 \cosh(-r + L) \cosh(-r + L)}$ 
> xi := (1+b*r^2)^(-3/2)*sinh(L-1)/6*cosh(r-1)^2*cosh(r-L);
xi :=  $\frac{\sinh(L - 1)}{6 (b r^2 + 1)^{3/2} \cosh(-r + l)^2 \cosh(-r + L)}$ 
> fr := diff(f,r);
fr := diff(f,1);
xir := diff(xi,r);
xil := diff(xi,l);

> l:=0;
l := 0
> L:=2;
sol:=fsolve([f,Wp], {r=0.81, b=0.05});
L := 2
sol := {b = 0.03406382360, r = 0.8355850293}

> L:=3;
sol:=fsolve([f,Wp], {r=0.81, b=0.05});
L := 3
sol := {b = 0.08650427219, r = 0.7835180270}

```



```

> restart;
rp := -f1/fr;
rpp := -(frx*rp^2+2*fr1*rp+f11)/fr;
rppp := -(frxx*rp^3+3*frrl*rp^2+3*frll*rp+3*frr*rp+rpp+3*frl*rpp+
frll)/fr;
Wp := xir*xrp*xil;
Wppp := xirrx*rp^3+3*xirrl*rp^2+3*xirll*rp+3*xirr*rp*rpp+3*xirl*xirr*xir*xirpp+xilll;

> f := 2*b*r/(1+b*r^2)+2*sinh(2*r-L-1)/5*cosh(r-1)/cosh(r-L);
f :=  $\frac{2 b r}{b r^2 + 1} - \frac{2 \sinh(-2 r + L + 1)}{5 \cosh(-r + L) \cosh(-r + L)}$ 
> xi := (1+b*r^2)^(-3/2)*sinh(L-1)/6*cosh(r-1)^2*cosh(r-L);
xi :=  $\frac{\sinh(L - 1)}{6 (b r^2 + 1)^{3/2} \cosh(-r + l)^2 \cosh(-r + L)}$ 
> fr := diff(f,r);
fr := diff(f,1);
fr1 := diff(f,r,1);
fr2 := diff(f,r,1,1);
frx := diff(f,r,r);
frl := diff(f,r,r,1);
frll := diff(f,r,r,1,1);
frl1 := diff(f,r,r,1,1);
frll1 := diff(f,r,r,1,1,1);
frll2 := diff(f,r,r,1,1,1,1);

> xir := diff(xi,r);
xir := diff(xi,r,1);
xirr := diff(xi,r,r);
xir1 := diff(xi,r,1,1);
xirr1 := diff(xi,r,1,1,1);
xirr2 := diff(xi,r,1,1,1,1);

> l:=0;
l := 0
> sol:=fsolve([f, Wp, Wppp], {r=0.8, L=2.1, b=0.08});
sol := {L = 2.597190816, b = 0.07596727744, r = 0.7926550122}

```

Fig. 14: Maple code to compute the bifurcation point (left panel) from (3.20) and the second-order bifurcation point (right panel) from (3.21), which corresponds to the switch between a subcritical and a supercritical symmetry-breaking bifurcation.

- [2] C. N. Chen, S. I. Ei, S. Tzeng, *Heterogeneity-induced effects for pulse dynamics in Fitzhugh-Nagumo-type systems*, Physica D, **382-383**(1), (2018), pp. 22–32.
- [3] H. Dankowicz, F. Schlieder, *Recipes for continuation*, in the book series *Computational Sciences and Engineering*, SIAM Publications, (2013), xv + 564 pages.
- [4] A. Doelman, R. A. Gardner, T. Kaper, *Large stable pulse solutions in reaction-diffusion equations*, Indiana U. Math. J., **50**(1), (2001), pp. 443–507.
- [5] A. Doelman, T. Kaper, *Semistrong pulse interactions in a class of coupled reaction-diffusion equations*, SIAM J. Appl. Dyn. Sys., **2**(1), (2003), pp. 53–96.
- [6] A. Doelman, T. Kaper, K. Promislow, *Nonlinear asymptotic stability of the semi-strong pulse dynamics in a regularized Gierer-Meinhardt model*, SIAM J. Math. Anal., **38**(6), (2007), pp. 1760–1789.
- [7] E. J. Doedel, A. R. Champneys, T. Fairgrieve, Y. Kuznetsov, B. Oldeman, R. Paffenroth, B. Sandstede, X. Wang, C. Zhang, *Auto07p: Continuation and bifurcation software for ordinary differential equations*, Technical report, Concordia University, 2007.
- [8] A. Gierer, H. Meinhardt, *A theory of biological pattern formation*, Kybernetik, **12**, (1972), pp. 30–39.
- [9] L. Harrison, D. Holloway, *Order and localization in reaction-diffusion pattern*, Physica A, **222**, (1995), pp. 210–233.
- [10] P. van Heijster, C. N. Chen, Y. Nishiura, T. Teramoto, *Pinned solutions in a heterogeneous three-component Fitzhugh-Nagumo model*, J. Dyn. Diff. Eq., **31**(1), (2019), pp. 153–203.
- [11] D. Holloway, L. Harrison, J. Armstrong, *Computations of post-inductive dynamics in axolotl heart formation*, Developmental Dynamics, **200**, (1994), pp. 242–256.
- [12] D. Holloway, *Reaction-diffusion theory of localized structures with applications to vertebrate organogenesis*, Ph. D. thesis in Chemistry, University of British Columbia, (1995).
- [13] A. Hunding, *Bifurcations in Turing systems of the second kind may explain blastula cleavage plane orientation*, J. Math. Biol., **25**(2), (1987), pp. 109–121.
- [14] D. Iron, M. J. Ward, J. Wei, *The stability of spike solutions to the one-dimensional Gierer-Meinhardt model*, Physica D, **150**(1-2), (2001), pp. 25–62.
- [15] D. Iron, M. J. Ward, *The dynamics of multi-spike solutions to the one-dimensional Gierer-Meinhardt model*, SIAM J. Appl. Math., **62**(6), (2002), pp. 1924–1951.
- [16] T. Kolokolnikov, S. Xie, *Spike density distribution for the Gierer-Meinhardt model with precursor*, Physica D, **31**, 132247, (2019)
- [17] T. Kolokolnikov, J. Wei, *Hexagonal spike clusters for some PDE's in 2-D*, to appear, DCDS-B, (2020).
- [18] T. Kolokolnikov, J. Wei, *Pattern formation in a reaction-diffusion system with space-dependent feed rate*, SIAM Review, **60**(3), (2018), pp. 626–645.
- [19] A. Krause, V. Klika, T. E. Woolley, E. A. Gaffney, *Heterogeneity induces spatiotemporal oscil-*

- 749 *lations in reaction-diffusion systems*, Phys. Rev. E **97**(5), 052206, (2018).
 750 [20] A. Krause, V. Klika, T. E. Woolley, E. A. Gaffney, *From one pattern into another: Analysis of*
 751 *Turing patterns in heterogeneous domains via WKBJ*, preprint, arXiv:1908.07219 [nlin.PS].
 752 [21] H. Meinhardt, *Models of Biological Pattern Formation*, Academic Press, London (1982).
 753 [22] K. Page, P. K. Maini, N. A. M. Monk, *Pattern formation in spatially heterogeneous Turing*
 754 *reaction-diffusion models*, Physica D, **181**(1-2), (2003), pp. 80–101.
 755 [23] K. Page, P. K. Maini, N. A. M. Monk, *Complex pattern formation in reaction-diffusion systems*
 756 *with spatially varying parameters*, Physica D, **202**(1-2), (2005), pp. 95–115.
 757 [24] W. Sun, M. J. Ward, R. Russell, *The slow dynamics of two-spike solutions for the Gray-Scott*
 758 *and Gierer-Meinhardt systems: competition and oscillatory instabilities*, SIAM J. App.
 759 Dyn. Sys., **4**(4), (2005), pp. 904–953.
 760 [25] J. C. Tzou, A. Bayliss, B. J. Matkowsky, V. A. Volpert, *Stationary and slowly moving localized*
 761 *pulses in a singularly perturbed Brusselator model*, Europ. J. Appl. Math., **22**(5), (2011),
 762 pp. 423–453.
 763 [26] J. C. Tzou, Y. Nec, M. J. Ward, *The stability of localized spikes for the 1-d brusselator reaction-*
 764 *diffusion model*, Europ. J. Appl. Math., **24**(4), (2013), pp. 515–564.
 765 [27] M. J. Ward, D. McInerney, P. Houston, D. Gavaghan, P. Maini, *The dynamics and pinning of*
 766 *a spike for a reaction-diffusion model*, SIAM J. Appl. Math., **62**(4), (2002), pp. 1297–1328.
 767 [28] M. J. Ward, J. Wei, *Hopf bifurcations and oscillatory instabilities of spike solutions for the*
 768 *one-dimensional Gierer-Meinhardt model*, J. Nonlinear Science, **13**(2), (2003), pp. 209–264.
 769 [29] M. J. Ward, J. Wei, *Asymmetric spike patterns for the one-dimensional gierer-meinhardt*
 770 *model: equilibria and stability*, Europ. J. Appl. Math., **13**(3), (2002), pp. 283–320.
 771 [30] J. Wei, *Existence and stability of spikes for the Gierer-Meinhardt system*, book chapter in
 772 *Handbook of Differential Equations, Stationary Partial Differential Equations*, Vol. 5 (M.
 773 Chipot ed.), Elsevier, (2008), pp. 489–581.
 774 [31] M. Winter, J. Wei, *On the Gierer-Meihhardt system with precursors*, DCDS-A, **25**(1), (2009),
 775 pp. 363–398.
 776 [32] J. Wei, M. Winter, *Stable spike clusters for the one-dimensional Gierer-Meinhardt system*,
 777 *Europ. J. Appl. Math.*, **28**(4), (2017), pp. 576–635.